8-2014

Design and Demonstration of a Two-Dimentional Test Bed for UAV Controller Evaluation

Ran Huang
Clemson University, rhuang2@clemson.edu

Design and Demonstration of a Two-dimensional Test Bed for UAV Controller Evaluation

A Master's Thesis
Presented to
the Graduate School of
Clemson University

In Partial Fulfillment
of the Requirements for the Degree
Master of Science
Electrical Engineering

by
Ran Huang
August 2014

Accepted by:
Dr. Timothy C. Burg, Committee Chair
Dr. Richard E. Groff
Dr. John R. Wagner

Abstract

A three degree-of-freedom (DOF) planar test-bed for Unmanned Aerial Vehicle (UAV) controller evaluation was built. The test-bed consists of an instrumented tether and an experimental twin-rotor, planar UAV mounted with a one DOF manipulator mounted below the UAV body. The tether was constructed to constrain the UAV under test to motion on the surface of a sphere. Experiments can be conducted through the tether, approximating motion in a vertical plane by a UAV under test. The tether provides the means to measure the position and attitude of the UAV under test. The experimental twin-rotor UAV and one-link on-board manipulator, were designed and built to explore a unified control strategy for Manipulator on VTOL Aircraft (MOVA), in which the interaction of UAV body dynamics with the manipulator motion is of primary interest. The dynamics of the propulsion unit was characterized through experiments, based on which a phase lead compensator was designed to improve the UAV frequency response. A "separate" controller based on independent nonlinear control of the VTOL aircraft and PD linear control of the on-board manipulator was designed as a reference for comparison to the unified MOVA controller. Tests with the separate controller show the negative effect that a coupled manipulator can have on the UAV body motion, while the tests on MOVA show the potential benefit of explicit compensation of the UAV and manipulator interaction.

Acknowledgments

I would like to express my gratitude to my academic advisor Dr. Timothy C. Burg for providing me the opportunity to participate in the UAV lab and for his invaluable guidance in my two years of study and research. I thank my committee members Dr. Richard E. Groff and Dr. John R. Wagner for their advice. I would like to acknowledge Mr. Peng Xu for his valuable suggestions and discussion about my research from which I have greatly benefited.

Last but not the least I would like to convey my special thanks to my parents for their unconditional support during my studies. I would also like to extend my thanks to my friend DanDan for her comforts and help during the difficult days.

Table of Contents

List of Tables

List of Figures

Chapter 1

Introduction

1.1 Background

1.1.1 Unmanned Aerial Vehicle

Small Unmanned Aerial Vehicles (UAVs), for example the quadrotor shown in Figure 1.1, are now extensively used in both civilian and military operations. The rapid development of microcontrollers and sensing technology have made it feasible to deploy UAVs in both types of applications. Among all the types of UAVs, small Vertical Takeoff and Landing (VTOL) aircraft have drawn increasing interest because of their distinct maneuverability advantages over conventional fixed wing aircraft in surveillance and inspection tasks. These tasks, such as searching, fire detection, crop surveillance, and traffic inspection, may require a vehicle that can loiter for detailed observation or fly close to fixed or moving obstacles. Modeling and control algorithms for VTOLs have been investigated in many scientific works. Proportional-integral-derivative (PID) controllers, with gain scheduling, are widely used in controlling commercial UAVs [8]. More refined control algorithms that con-

sider the complete nonlinear system dynamics are under development. Sophisticated techniques, such as integrator back-stepping approach, can be applied in the design of such control systems [5].
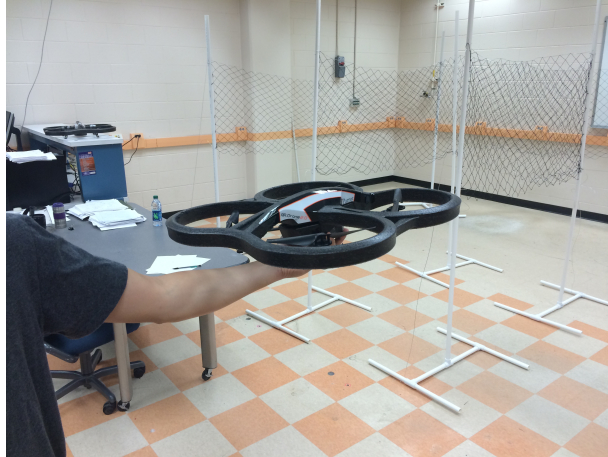
Figure 1.1: The Parrot AR Drone 2.0 is an example of the current class of small UAVs available for civilian use.

1.1.2 Mobile Manipulator

Manipulators or robotic arm mechanisms are similar to human arms that can grasp and move objects. They can be programmed to operate autonomously or to be manually controlled. A large number of manipulators have been designed in the last sixty years and many of them have been widely used in industry. Manipulators deployed on mass production lines are productive and helpful, but their fixed work space has severely limited their suitable applications. In order to tackle new problems and expand the flexibility of manipulator arms, manipulator arms have been combined with mobile robot platforms.

Mounting a manipulator on a mobile platform to produce a mobile manipulator is not a new idea, there have been research groups building mobile manipulators for many years [16]. Currently most mobile manipulators are built on ground vehi-

2

cles and have been able to perform various practical tasks like bomb defusing and space exploration. However, due to limitations of the mobile platforms, most of these manipulator systems can only work on ground with smooth terrain. Also, large supportive devices are demanded in large architectural structure inspections and constructions, such as factory chimney tests or tall building outside wall maintenance, when ground-based mobile manipulators are used.

1.1.3 UAV Borne Manipulator

In most current UAV applications, the UAV is used only as a carrier for environment sensors or a video acquisition device. The idea of mounting a robotic manipulator on a UAV such that it is able to interact with other objects reveals great potential for UAVs in even more applications.
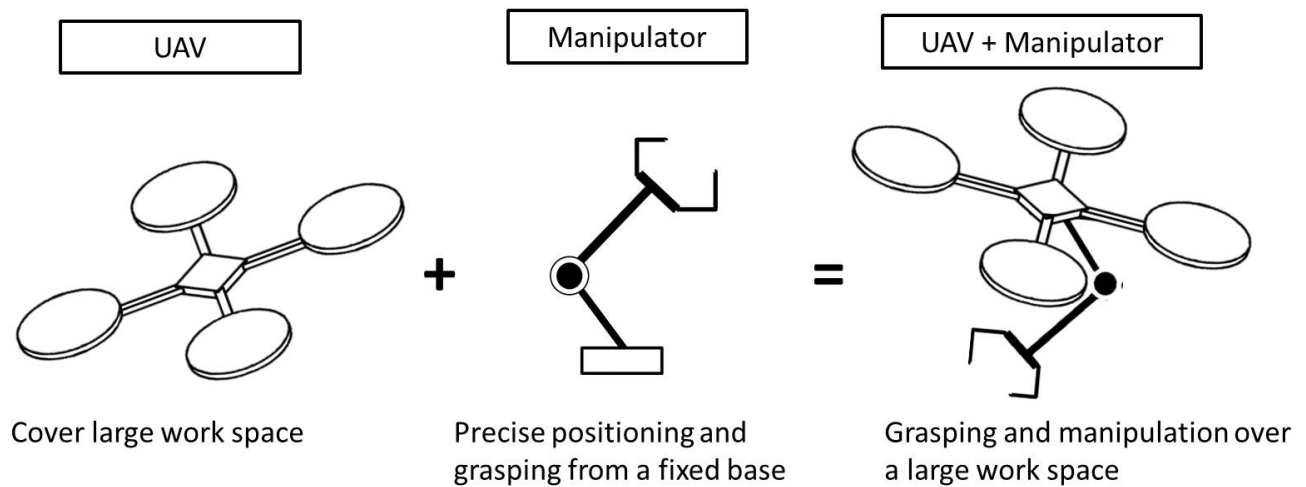
Figure 1.2: The primary advantage of mounting a manipulator arm on a UAV is the nearly unlimited workspace.

Interest is developing in aerial manipulators. The obvious advantage is that the workspace is extended from a small 3D volume to the whole space where the UAV

can travel (Figure 1.2). Such a system has the dexterity of the manipulator plus better mobility compared to the ground-based mobile manipulator. As a host platform, the VTOL can be deployed at places that are inaccessible for ground mobile manipulators, allowing the manipulator attached on the VTOL aircraft to interact with the remote environment. Potential tasks include tall buildings or bridge maintenance, material sample collection from complex terrain, and package delivery (Figure 1.3). Even for those tasks that are currently undertaken by ground manipulators, the agility of VTOL aircraft in narrow spaces and the fast travel speed regardless of terrain complexity could provide better performance.
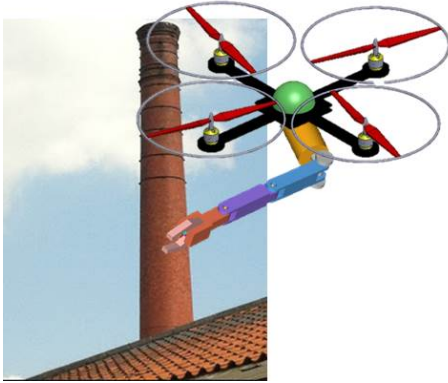
(a) Factory chimney inspection
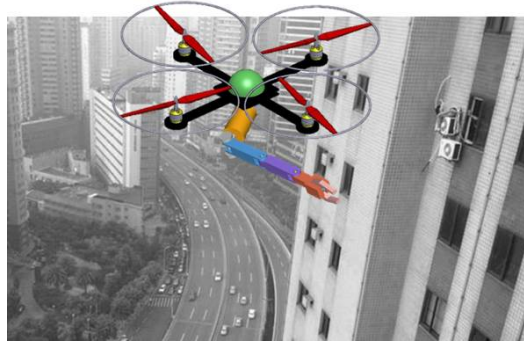
(b) Tall building outside wall maintenance

(c) Fighting a fire

(d) Defusing a bomb

Figure 1.3: Potential applications of Unmanned Aerial Vehicles (UAVs)

While equipping VTOL with robotic arm has great potential in various applications, very few control algorithms are developed to harness the performance of such an integrated system efficiently. Challenges still exist before VTOL aircraft and robotic arms can truly be integrated together and fulfill the potential of such systems. One important issue has to do with the underactuated nature of the VTOL

aircraft. Underactuated refers to a system in which not all of its degree-of-freedom (DOF) could be independently controlled, there are fewer independent control actuators than the total DOF. Specifically for the quadrotor aircraft, among the six degree-of-freedom of the VTOL, only four of them can be controlled separately while the x- and y- position are not directly controllable. The unique problem of controlling an aerial vehicle with an attached manipulator is that the internal force and torque generated by the interaction between the arm and the host VTOL may not be negligible depending on the relative mass of the two subsystems. Such interaction adds to the complexity of the dynamics model of the whole system and is difficult to stabilize when designing a controller. Secondly, operating from a hovering VTOL aircraft makes the end-effector difficult to perform fine motions to target the object of interest precisely.

Another issue in constructing a UAV borne manipulator is the flight time. Since for most application scenarios, like searching and rescuing, VTOLs equipped with robotic arms are required to operate through a long distance, the flight time is one of the most critical factors. While a heavy host VTOL, renders the system less susceptible to interaction with the onboard manipulator, it will consume more energy thus resulting in shorter flight time. The manipulator design must balance functionality (often redundancy) of the manipulator against weight of the manipulator. Redundant links, although helpful to position the robot at arbitrary configurations for manipulation tasks, add to the total weight and draw extra energy while operating and transporting.

There are some researchers trying to address the above issues. The GRASP research team of University of Pennsylvania has used a fleet of quadrotors to perform cooperative assembly work [6]. Pounds *et al.* used PID controllers to stablize the host UAV, taking the change of load mass as disturbance [8]. They determine a

bound within which changing load mass will not destabilize the aircraft. However only a grasper is attached under the aircraft for object retrieval and the accuracy of tracking trajectory while carrying an object is not discussed in this paper. Another group has mounted and controlled a multi-link manipulator on a VTOL UAV [1]. Redundant degrees-of-freedom (DOF) for the manipulator or host UAV are required to compensate for the interactive torque within the system, i.e. extra weight and complexity is added to the system in order to compensate for what is likely a control design issue. Yet the total weight along with the cost will increase for the redundant actuators, which are not discussed in the paper either.

1.1.4   New Design of Manipulator on VTOL Aircraft(MOVA)

In regard to the above issues, one efficient way to extend the flight time is to minimize the weight of the manipulator, that is, use only the necessary number of actuators for the system. Specifically for a quadrotor, utilize the four degree-of-freedom VTOL aircraft coupled with a two degree-of-freedom manipulator to generate a six degree-of-freedom aerial manipulator system.

A challenge of realizing the potential benefits of the VTOL + manipulator system involves managing the interaction of the onboard manipulator and the VTOL aircraft–the dynamics of both subsystems may be profoundly affected by each other, depending on relative masses and moment of inertia. When deriving a dynamic model of the complete system by directly applying Euler-Lagrangian approach, coupled terms that neither belong to the aircraft nor the manipulator are produced. These complex coupling terms represent the interaction between two subsystems and add to the difficulty in control algorithm design [14].

The typical control design approach has been to acknowledge that this phe-

nomenon exists but design controllers that only implicitly address these forces, e.g. design an aircraft body controller that is robust to these disturbances. To explicitly approach the challenge, Xu *et al.* designed an innovative aerial mobile manipulator, referred to as MOVA [12], which stands for Manipulator on VTOL (Vertical Take-Off and Landing) Aircraft. In preparation for developing MOVA control algorithm in 3-dimensional (3D) space, the dynamic equation and control algorithm of 2D model was investigated in Xu's work. The planar MOVA system has minimal number of joints for the end-effector to achieve trajectory tracking. Figure 1.4 illustrates the difference between a redundant manipulator and the MOVA approach. Through virtual manipulator method, dynamics of the MOVA system are transformed into a form that has decoupled translational and rotational dynamics. The resulted dynamic equations facilitate the controller design. After deriving the decoupled dynamic equation, the paper describes a unified back-stepping controller for the integrated system.
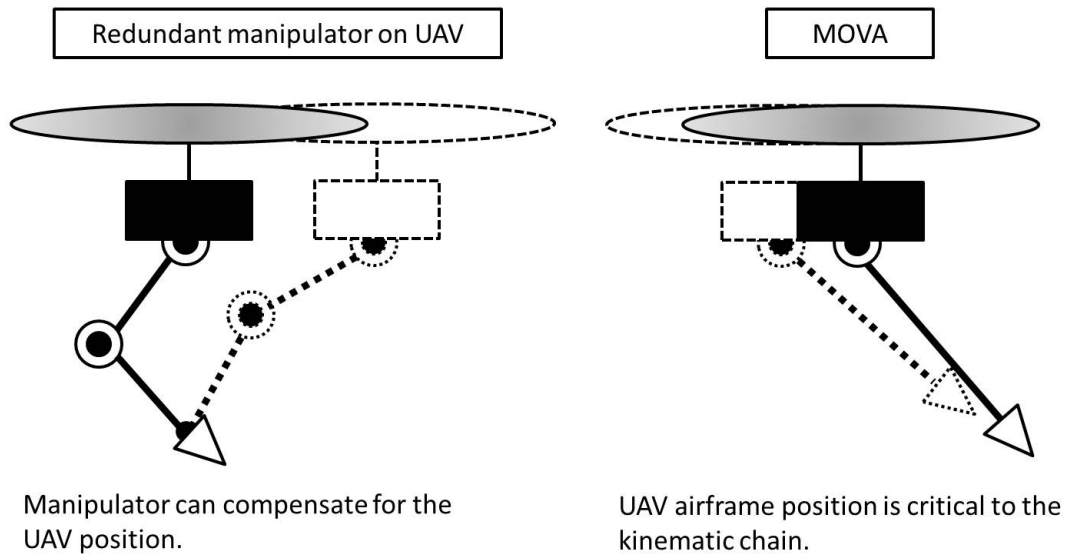
Figure 1.4: An illustration of difference between a redundant aerial manipulator and a MOVA system.

1.2 Problem Statement

Controlling the VTOL aircraft and the manipulator through one unified controller is a new idea, it is very appealing to run physical tests for the system and demonstrate the interesting points in the MOVA control algorithm such as the active compensation for interactions between the VTOL and the manipulator. An experimental test-bed for validation of the MOVA system is needed.

1.2.1 Test bed Motion Constraint

Many UAV tests are performed using outdoor test facilities where reliable on-board navigation systems are required, such as GPS, gyros, accelerometers and magnetometers. There are great advantages to outdoor experiments yet they can be considerably expensive due to the number of the sensors and data acquisition devices. Outdoor UAV experiments must be performed in a wide open area by well trained personnel and are vulnerable to weather conditions. Compared to indoor tests, all those factors render the outdoor tests less appealing to researchers subjected to limited funding or work site constraints. By using small or mini UAVs and using external (off-board) position and attitude estimate, indoor tests could be performed at anytime, and experimental results can be analyzed instantly.

Considering potential crash scenarios during the tests, the safety of personnel and devices around the test become the most important factor when deciding on the type of facility to use. A fail-safe configuration and simple mechanical design are desirable for a test bed.

A tether configuration that constrains motion of a UAV under test within a 2-dimensional (2D) plane is proposed. Due to the difficulty of physically realizing a 2D plane motion, a spherical approximation is made by connecting the UAV to a

fixed point through a long radius. Q8 Hardware-In-the-Loop (HIL) Board and xPC Target are used to process the feedback signal from sensors incorporated in the tether and command the outputs. Simulink® is used to implement the control algorithm.

1.2.2   UAV Platform for Testing

Among all the VTOL vehicles, quad-copters, or also called quadrotors are more suitable than tail rotor helicopters as indoor test platforms. A quadrotor is lifted by two sets of identical and symmetrically arranged propellers. Other than simplicity of control, it has simpler machine construction than a comparably scaled helicopter as well as smaller sized propellers, which could reduce the damage caused should the vehicle is out of control.

At the moment there are no commercial UAV quadrotors mounted with robotic arms on the market. Such test beds when needed are usually modified and developed from a few quadrotor platforms. One of the most notable platform models is the AR.Drone produced by Parrot. There are also Hummingbird, Dragonflyer and a few other commercial quadcoptors that are suitable for research. Some of the most popular commercial quadrotors used by research institutes are listed in Table 1.1.

The AR. Drone is favored by many research groups. It has two cameras therefore and could be used to perform vision experiments. But its frame size is rather too large for indoor experiments. Its limited lifting force and compact body size limit the ability for further modifications. While the Hummingbird, IRIS and Dragonflyer are compact in size they are more expensive.

Although the above listed products demonstrate good versatility with Global Positioning System (GPS) and provide on-board micro-controllers for different levels user customization, they are mostly for outdoor experiments and many of the sensors

Model	Size	Features	Price (USD)
A.R. Drone 2.0	820mm × 820mm	1. Equipped with camera of 1280 × 720 2. Triple axis gyroscope 3. Triple axis accerlerometer 4. Triple axis magnetometer 5. Pressure sensor 6. Ultrasound sensor	$ 200 or above
Hummingbird	540mm × 540mm	1. Autopilot developing tool 2. Extendable 3. Compact size suitable for indoor test 4. Triple axis magnetometer	$ 500 or above
IRIS	600mm × 600mm	1. Programmable autopilot 2. Magnetometer	$ 750 or above
Dragonflyer Shadow	502mm × 502mm	1. Flight data recorder 2. Accelerometer 3. Gyroscope 4. Pressure sensor	$ 2995 or above

Table 1.1: List of off-the-shelf quadrotors

on-board (GPS and magnetometer) appear to be useless for indoor tests. More importantly the unmodifiable mechanical configurations allow neither extra mounting points nor larger lifting force for on-board robotic manipulator.

A planar 2D test bed of a small UAV + manipulator is proposed. The test bed consists of a three degree-of-freedom, two dimensional host VTOL and a single link manipulator. Two propellers are used because redundant actuators yield undesirable torque about the yaw axis, which can lead to instability. The UAV and manipula-

tor, along with the proposed tether, constitute a complete test bed for the UAV + manipulator controller evaluation (Figure 1.5).
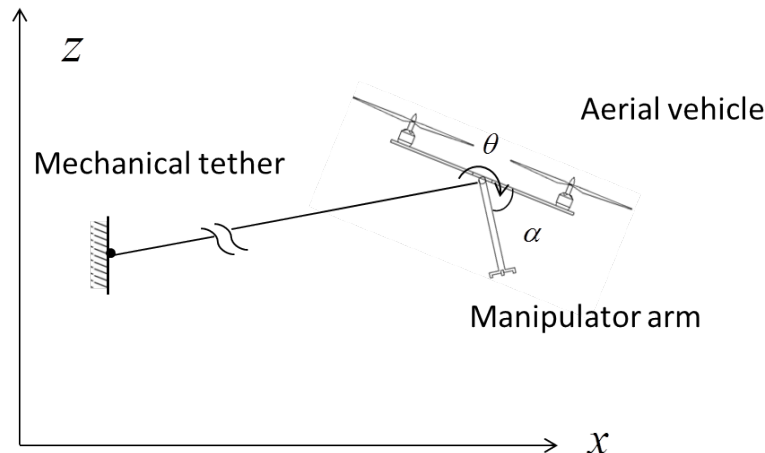
Figure 1.5: 2D planar test bed allows planar motion (x- and z- directions) and roll (θ) and rotation angle (α) of the manipulator.

1.3   Related Works

While there are no established test beds that can be directly used for the MOVA system, the development of an open source UAV platform would allow researchers to adapt and modify UAVs cater to specific aims. The GRASP research team of University of Pennsylvania has developed a test bed to test multirobot aerial control algorithms using the Hummingbird quadrotor [6]. Another group modified Q4 Dragster frame from Lipoly.de to support a direct approximate-adaptive control [7]. The quadrotor was constrained in Z- direction by being mounted on a spherical bearing allowing only yaw and limited rolled and pitch motion. In Tayebi and McGilvray's paper [9], experimental tests were performed on a modified Draganflyer III from RC Toy. A stationary ball joint base is attached to the quadrotor and a dSPACE DS1104 R&D board is used to control it. In their experiments, motor speed is measured by

Hall-effect sensors. Hoffman, Goddenmeier and Bertram used a test bed mounted on a gimbal to compare proportional-integral-derivative (PID) and Integrator back-stepping controllers [2]. Instead of being modified from commercial quadrotor, the test bed is not a real quadrotor but constructed using light weight frame along with electronic components. Yu and Ding designed a test bench mounted on a fixed base through a sphere joint [11]. The test bench also includes 6 axes torque/force sensor to measure dynamics of motor-propeller subsystems.

All of the above test beds constrain the main body (Figure 1.6) at a fixed point. Such constraints keep the test bed safe to operate. But in order to fully evaluate the control algorithm, the test bed should also allow the aircraft to track trajectories in the space and demonstrate the action of a controller under a real flying conditions. Ability to record flying data such as pitch angle and translational speed is also required.
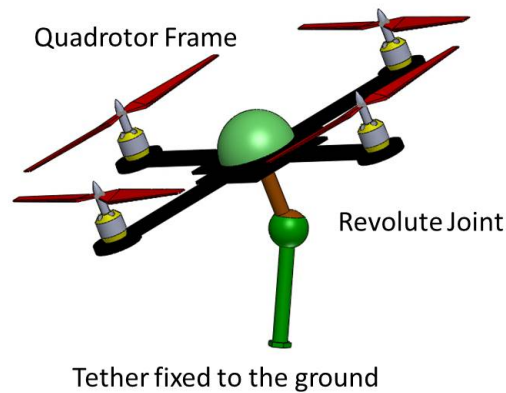
Figure 1.6: Testbed Schematic

In addition to indoor VTOL test beds, other research groups have mounted multi-link arm on outdoor UAVs. The Vision and Control Group from University of Seville presents a quadrotor with an arm for assembly tasks [3]. The new platform is used to test an Integrator back-stepping controller that takes into account the motion

of the arm. Korpela *et al.* describes a design of miniature gantry crane mounted on a large UAV [4].

In sum, indoor test beds have the distinctive advantage of low cost and immunity to weather influence. Many research groups use test beds modified from quadrotor or multi-rotor because of their simple mechanical construction control convenience. But most of the self-modified test beds can only measure flying attitude instead of demonstrating a real flying condition. Although commercial quadrotors for hobbyists provide good versatility and refined frame, they have little room for modification to meet user specified requirements. Building a new test bed is low cost and could be modified according to future needs. Certain constraints should be applied to the VTOL vehicle to keep the test bed operating in a safe area. The constraints should also allow the aircraft to fly sufficient freedom for complete testing.

1.4   Organization

The first chapter provides a background introduction of UAV and aerial manipulator. In particular the integrated UAV and manipulator system, referred to as MOVA, is presented. The need for a MOVA test bed is stated and some related test beds are introduced. The overall design of the proposed work is thus motivated.

In Chapter 2, system architecture is illustrated following a top down functional decomposition method. All functional modules are described, including two attitude position measurement methods: 1). using encoders in the mechanical tether that are attached to the host VTOL helicopter and manipulator actuator to measure and derive position of the end-effector; and 2). via image processing using a camera as a sensor for position measurement. Comparison between the two methods are performed and results are discussed. In Chapter 3, a controller that applies the same

back-stepping technique as MOVA but based on a conventional Euler-Lagrangian approach derived dynamic model is described and implemented. The performance of the controller is compared with the MOVA controller. Results of maintaining at fixed positions and tracking different end-effector trajectories are presented. The last chapter summarizes the achievements of the proposed work. Possible improvements on the test bed and suggestions for future work are presented.

Chapter 2

2D Planar Test bed Design

The design of the test bed instrumentation and hardware are described via functional decomposition in this chapter. The first section introduces the system architecture. Five subsystems that constitute the test bed system are introduced and the requirements are defined. The second section presents the control software and hardware: the Q8 hardware-in-the-loop (HIL) board, the Host PC and the software environment Mathworks xPC Target. The air frame design and the material selection are explained in the third section. The tether used to constrain the UAV movement, position sensor and single-link robotic arm module are detailed. The following section focuses on the propulsion module, the brushless DC drive motor and electronic speed controller (ESC) and its control interface are described in this section. Tests that measure propeller static thrust and measurement of the frequency response are elaborated in Section 5. In the last section, two methods of attitude estimation, rotary encoder at the end of the tether and a camera-based system, are described and their performances are compared and discussed.

2.1   System Architecture

The objective is to design and build a two-dimensional test bed for UAV controller testing and a prototype 3 DOF Manipulator On a VTOL Aircraft (MOVA). In order to execute the design process, the system is divided into modules that serve specific functions. The two main systems are the instrumented tether, including UAV control hardware and software, and the UAV under test. Five subsystems and their interactions that define the system architecture are presented in Figure 2.1. The control algorithm runs on the xPC Target PC and interacts with the hardware through the Quanser Q8 board. The Q8 board reads in VTOL position and VTOL attitude from position sensors, and issues commands to the robotic arm and propulsion units to bring the end-effector to a desired position. Requirements of each subsystem are detailed in the following subsections.
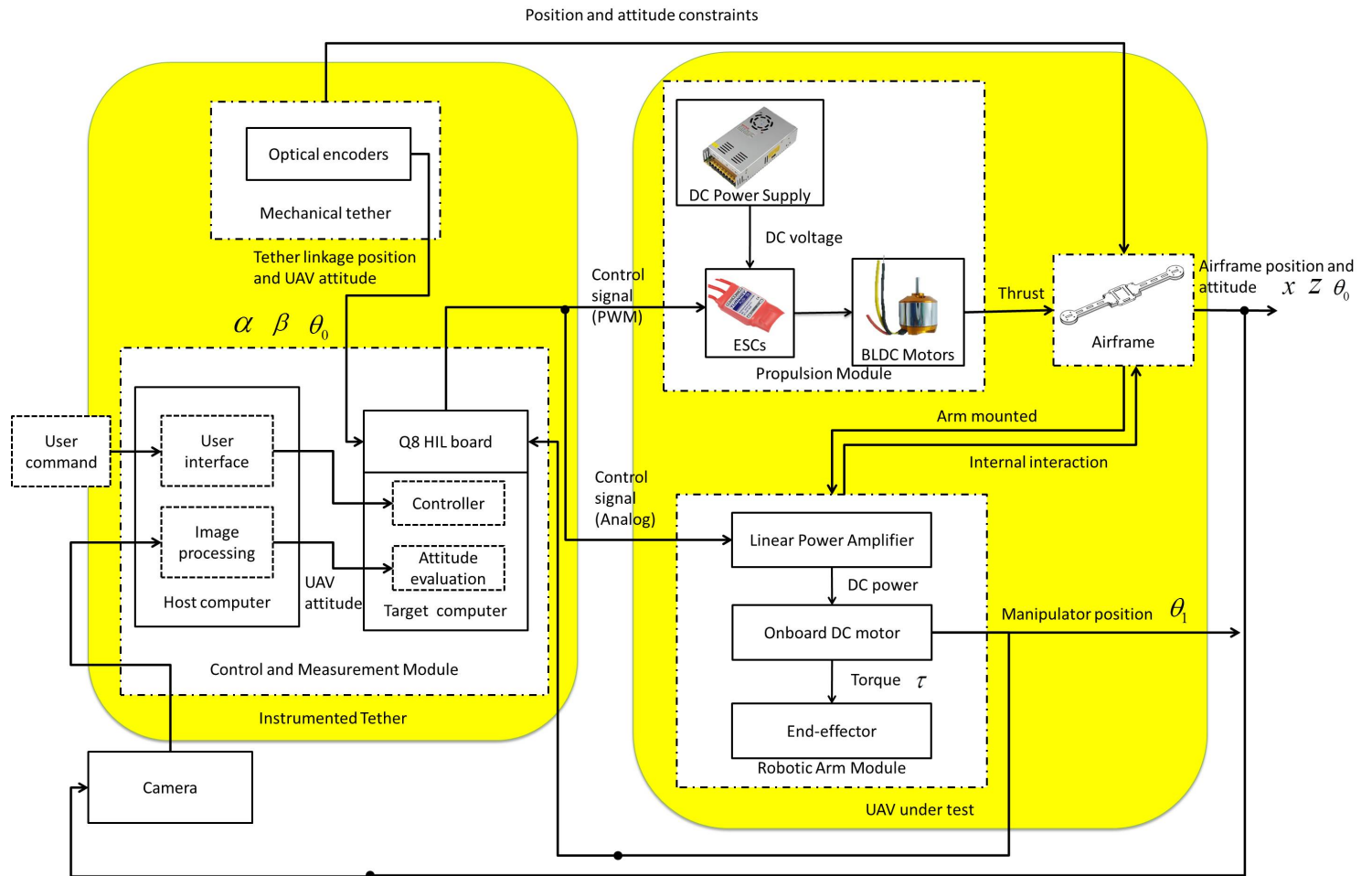
Figure 2.1: System architecture

2.1.1 Control and Position Estimation

To implement UAV controller on the test bed, a data acquisition and control platform is required to take in multiple sensor inputs, estimate the system states, evaluate the control algorithm and output analog or digital commands to the UAV under test. The control system should be able to generate command signals at least 100 times per second to guarantee sufficient flight control. An algorithm, implemented in the control system software, will perform system position evaluation. The inputs and outputs of the control module are listed in Table 2.1.

18

Module	Control and Measurement Module
Inputs	Quadrature TTL signal from encoder with 4 channels
	VTOL roll angle data from encoder (+90 to -90 degree)
	Manipulator direction from user
	Tether linkage position α and β
	UAV attitude θ_0
	Data from camera
Outputs	Pulse width modulation (PWM) signal for servo control (standard hobby servo interface)
	Analog control signal: -5V to +5V with at least 10-bit resolution
Functionality	Input sensor feedback, derive system position, compute and execute control algorithm

Table 2.1: Control and measure system functionality

2.1.2 Instrumented Tether

A tether will be designed to estimate the motion of the airframe and constrain the range of motion of the UAV under test. The system transnational position and sensing devices should be incorporated into the tether. Encoder sensor will be included in the tether but may add significant weight. An alternate sensor such as a camera may be feasible but may introduce extra noise to the system and be constrained by update rate. This alternate sensing approach will be investigated during the design process and a comparison test will be performed. For a sufficient position feedback, the position sensor and attitude sensor should have a resolution of at least 5 mm and 0.02 radian respectively.

2.1.3 Airframe

The air frame serves as a platform upon which the propulsion module and arm module are built. The frame should be compact and light weight. Appropriate rigidness is also required for the MOVA to survive vibration or even minor impact.

Module	Instrumented Tether
Inputs	Position of UAV under test
Outputs	TTL signal from encoder or voltage variation that can be recognized by the control board Position measurement resolution of 5mm Angular resolution of 0.02 radian Constrained spherical motion of 1 m radius
Functionality	Constrain motion at undesired direction and provide Real-time measurement of the MOVA position and attitude change

Table 2.2: Instrumented Tether Requirements

Module	Airframe
Inputs	External thrust F and torque τ
Outputs	VTOL position and attitude
Functionality	Serve as a platform for MOVA system construction

Table 2.3: Airframe requirements

2.1.4 Propulsion Modules

The propulsion module provides the thrust to the airframe to hover and travel in a plane. As a general rule, the maximum thrust generated by the propulsion unit should be twice the flying weight [17]. Accurate thrust control to follow the command from the control board is also needed. Based on experience on past projects, commercial, off-the-shelf electrical speed control and brushless motor are standard for small aircraft because of their high ratio of performance to cost.

Module	Propulsion Module
Inputs	Pulse Width Modulation (PWM) signal 12V DC voltage
Outputs	Thrust at least twice the total weight of the UAV under test
Functionality	Generating thrust and torque for VTOL to hover and change attitude

Table 2.4: Propulsion module requirements

2.1.5 Single-link Robotic Arm Module

The single-link robotic arm should possess appropriate mass and rotational inertia such that the interaction between the VTOL and arm can be observed while the VTOL is hovering. A DC motor is the most likely candidate as the arm actuator because of its compact size, high reliability and simple control. For configuration simplicity, a motor with built in encoder to measure the arm position is preferable. A programmable voltage amplifier is needed to transform AC supply voltage and the control signal into an appropriate DC voltage for the motor.

Module	Single-link robotic arm module
Inputs	120V AC voltage to the amplifier
	Analog control signal from the control board: -5V to +5V
Outputs	End-effector position as quadrotor encoder output
Functionality	Represent the robotic arm in the MOVA system

Table 2.5: Single-link robotic arm module

2.2 Control System

Q8 Hardware-in-the-Loop (HIL) Board and xPC Target$^{\text{TM}}$ are used as the real-time control system of the test bed. This hardware/software system is standard in the controls and robotics laboratory and was selected without additional consideration.

2.2.1 xPC Target$^{\text{TM}}$ and xPC Target Workstation

xPC Target$^{\text{TM}}$ is a real-time software environment from MathWorks Inc. which runs on a computer workstation without an operating system (eg. Microsoft Windows). It allows the user to run Simulink$^{\circledR}$ generated models in a separate PC based

workstation and provides a library of I/O drivers and a real-time kernel. The features of real-time monitoring, parameter tuning, and data logging make it an ideal environment for a control system test bed.

xPC Target software requires a Host computer, a Target computer and compatible I/O boards. The I/O board will be introduced in next subsection. Simulink models and executable code are constructed on the Host computer and then downloaded to the target computer for execution. In the proposed work, a Lenovo Y580 laptop computer is used as the Host computer.

2.2.2   Q8 HIL Board

The Quanser Q8 Hardware-In-the-Loop (HIL) board serves as an I/O board in the control system. It reads in system states and outputs control signals. The Q8 board is a peripheral component interconnection (PCI) based device that offers wide variety of I/O abilities (Table 2.6). Q8 HIL board has two parts-the main card and the terminal board. The main card (Figure 2.2a) is inserted into a PCI slot on the mother board of the Target workstation. The main card connects, through two 44-pin ribbon cables and one 50-pin ribbon cable, to the Q8 terminal board (Figure 2.2b), which has all the interfacing connectors. The input/output ports on Q8 HIL terminal card used in the proposed work are listed in Table 2.7.

8 x 14 bit Analog Inputs
8 x 12 bit D/A Outputs
8 Quadrature Encoder Inputs
32 Programmable Digital IO Channels
2 x 32 bit dedicated Counter/ Timers
2 External Interrupt sources
32 bit, 33MHz PCI Bus Interface

Table 2.6: Available I/O ports on Q8 HIL board
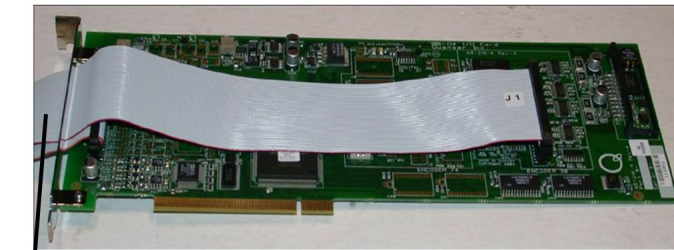
To the terminal board

(a) main board

From Q8 board

Analog Out (D/A) Channels

Analog In (A/D) Channels

Digital I/O Ports

Encoder Channels

Ext Interrupt and Signal Pins (PWM,Watchdog)
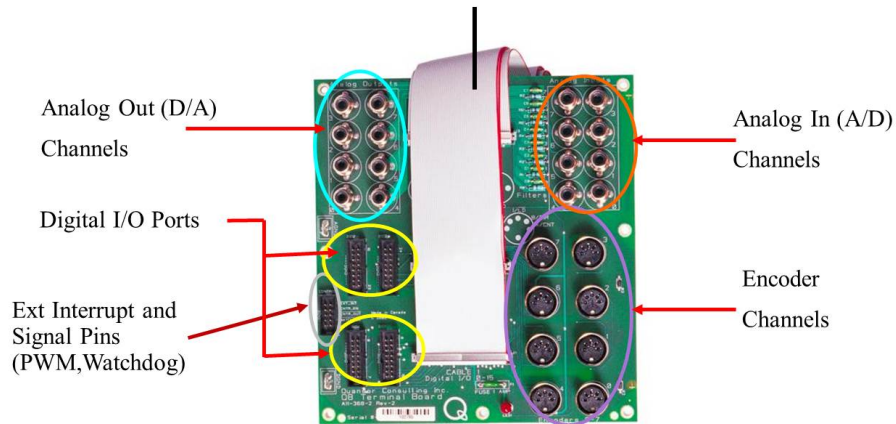
(b) terminal board

Figure 2.2: Q8 HIL board

2.2.3 Control Software

MATLAB Simulink is used to create a model of the control system. The model is then compiled as executable code and downloaded from the Host PC to the xPC Target workstation through an Ethernet connection. The model is run by xPC Target in real time, which communicates through the Q8 HIL board with test bed hardware, receiving sensor inputs and issuing commands. While the model is running, data can be stored in the memory of the Target workstation for offline analysis or shipped back to the host laptop for real-time display. A schematic of the control system is shown in Figure 2.3. Some sensors, such as the camera, can operate from the Host computer

23

I/O ports	Functionality
4x Encoder input	Recieve MOVA position (2 ports)
	Receive MOVA attitude
	Receive robotic arm position
1x Analog output	Issue voltage signal to onboard arm actuator
Counter/Watchdog output	Issue pulse width modulation signal to control brushless motor

Table 2.7: Q8 HIL board I/O used in the test bed

and the data is then transmitted to the control program on the Target computer
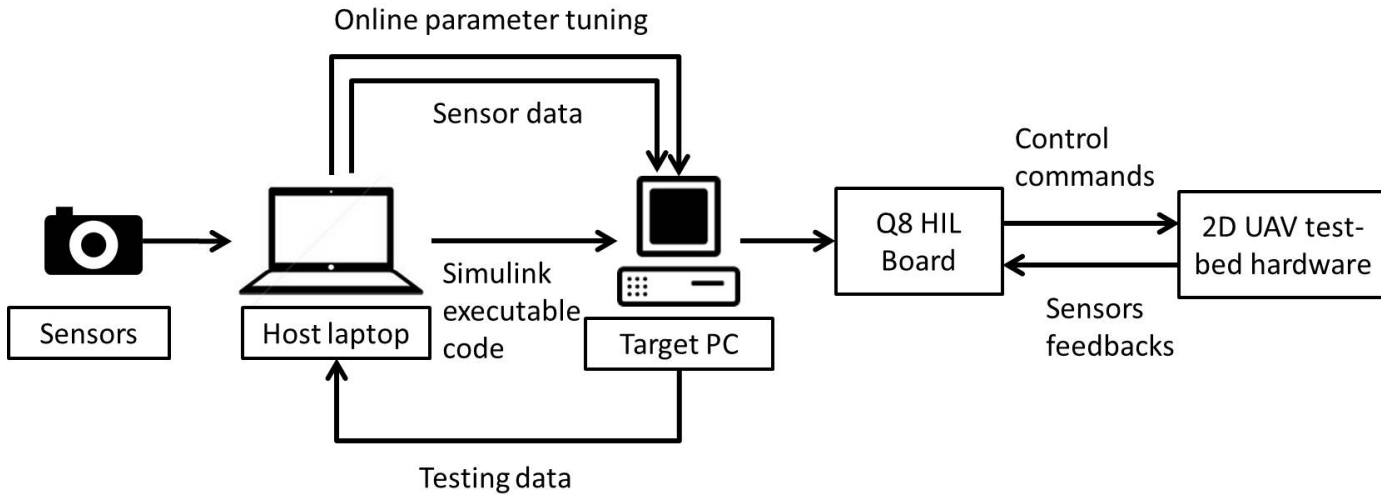
Figure 2.3: HIL control system using xPC Target

2.3 Instrumented Tether

Considering it is difficult to achieve a strictly planar movement, a spherical approximation is proposed. The aerial vehicle's motion is constrained by a tether which consists of a lightweight rod with a gimbal fixed to the ground at one end, and the other end is a rotary joint that provides the mounting point for the UAV under test. Such a connection constrains the yaw and pitch movement, leaving only the roll rotation to be performed by the MOVA. The tether is designed to be 1000 mm long,

and the airframe movement range is a 800×800 mm rectangle. The approximation along the x-axis is shown in Figure 2.4.
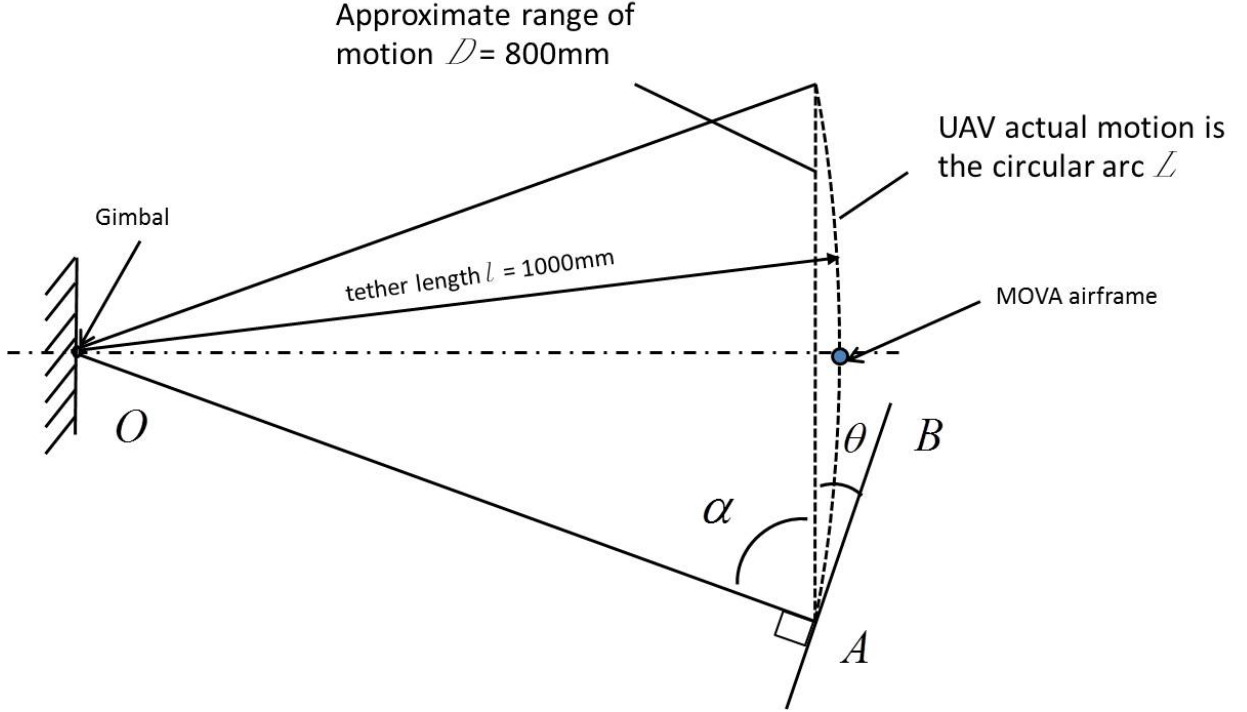
Figure 2.4: A schematic of spherical approximation of linear motion. Line AB is the tangent line to the circular arc L at point A.

The angle θ dictates the approximation of the linear motion. That is the smaller θ is, the more the actual arc approximates the imaginary line. Based on the law of cosines, $l^2 = l^2 + D^2 - 2lD\cos\alpha$ $\cos\alpha$ can be found by

$$\cos\alpha = \frac{D}{2l} = 0.4. \tag{2.1}$$

As tangent line AB is perpendicular to the radius OA, $\cos\alpha = \sin\theta$.

$$\theta = \sin^{-1}0.4 = 0.411\text{radian}. \tag{2.2}$$

25

A one-meter hollow fiberglass rod, made from the front part of a Zebco 202K fishing rod, is used to construct the tether linkage. Two Tohoku Ricoh DC motors, with optical encoders are assembled orthogonaly (Figure 2.5) to form a universal joint to connect the linkage to the ground. The motors are chosen to provide mechanical support and measure the airframe positions with the encoder (they are passive and not used to move the airframe). One of the advantages of the motor is that it has no gear box, and the output shaft is directly connected with the encoder and is supported with ball bearings, therefore the friction generated from motor's internal transmission can be neglected. One Tohoku Ricoh motor is fixed to the ground with its output shaft rotating freely. Through a shaft mounting hub, the base motor shaft is fixed with an acrylic made "L" shaped bracket, on which another motor is mounted. Detailed design dimensions are provided in Appendix B.
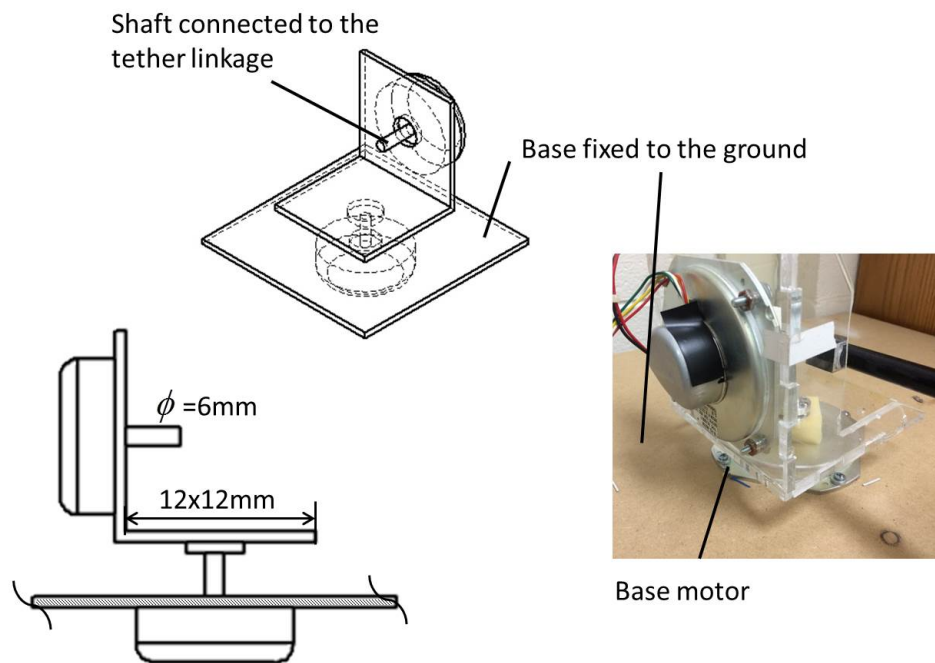
Figure 2.5: Two motor assembled as a universal joint

The other end of the tether linkage connects to the 2D MOVA. As the 2D

MOVA moves up and down (along z- axis), the upper motor shaft is turned. Likewise the base motor shaft turns as the linkage moves sideways (along the x- axis). Through this mechanism, the position of UAV under test in a plane can be computed from the measurement of the motor encoders. Given that they are quadrature encoder resolution of 400 counts square wave per revolution, the position measuring resolution is computed as:

$$r = \frac{2\pi}{4 \times 400} = 3.925 \text{mm/count.} \tag{2.3}$$

Therefore the position sensor meets the requirement in section 2.1.2.

The tether linkage end that connects to a UAV under test has an outer diameter of 8 mm. Two ball bearings with inner diameter of 8 mm are utilized to form the rotating joint between the 2D MOVA body and the rod to allow unconstrained roll motion. A bracket made of acrylic integrated into the airframe design, is used to secure the bearings. The mechanism (shown in Figure 2.6) prevents movement around the yaw and pitch axes.

Figure 2.6: End of tether rotary joint connection

2.4 Planar MOVA Airframe and Single-link Robotic Arm Design

The planar MOVA host airframe is constructed as "half" of a quadrotor. It is slightly different from simply dividing a quadrotor, in that it has two symmetrically arranged propellers. They are used i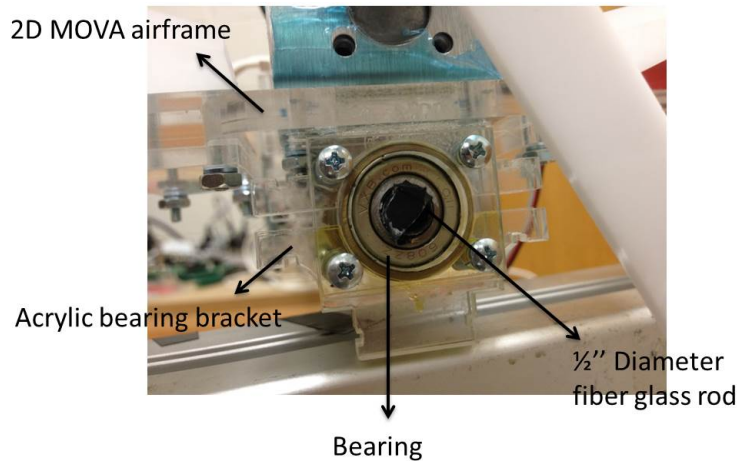n flight control to provide the twisting torque and lift force. The 2D MOVA can only fly along the x-axis and y-axis, in a plane, by adjusting rolling angle and thrust. An on-board actuator will be added to construct a single-link robot. A robotic arm with mass comparable to the host UAV is attached on the actuator. The 2D planar MOVA has 3 DOF from UAV + 1 DOF from manipulator = 4 DOF.

2.4.1 Airframe Design

Weight plays an important role in the UAV design. With two propellers the UAV's weight-to-thrust ratio would be less than half of that of the quad-copter. Enough thrust margin for good maneuverability could be guaranteed by using lightweight material and appropriate mechanical design. Another mandatory requirement is machinability-the airframe should be easily modified or shaped to meet any special needs.

Different materials have merits that help to meet the above requirements. Three materials are considered in the design—acrylic, aluminum and carbon fiber. Their properties are listed in Table 2.8. Aluminum and carbon fiber are favored by aviation hobbyists for their durability. Yet the aluminum is too heavy for a mini indoor test bed while the carbon fiber tubes are difficult to machine. On the other hand, the acrylic is light weight, has appropriate strength and can be easily cut into

desire shape by a laser cutter. Therefore the acrylic is suitable for the frame and was chosen as the only material used in the frame. All acrylic parts in this work were machined using the Versalaser Portable Desktop Laser Engraver, manufactured by Universal Laser System.

Material	Density	Strength
Aluminum [22]	2.7 $\mathrm{g\,cm^{-2}}$	High
Carbon fiber [23]	1.55 $\mathrm{g\,cm^{-2}}$	High
Acrylic [25]	1.18 $\mathrm{g\,cm^{-2}}$	Medium

Table 2.8: Material comparison

Given the limited thrust of only two propellers, the frame of the UAV is designed in a most efficient way. That is, the frame is designed to be as narrow as possible to support only necessary devices such as the end-effector actuator. To minimize weight the power supply and the control board will be off-board the UAV. The frame is designed as a symmetric "dumbbell"" shape with a rectangle at the middle (Figure 2.7). The motors are mounted on the end of each arm. Two identical frame layers are cut and assembled together through two ribs to enhance the rigidness of the structure. The length of the frame, which is also the distance of two propellers was set to 300 mm.
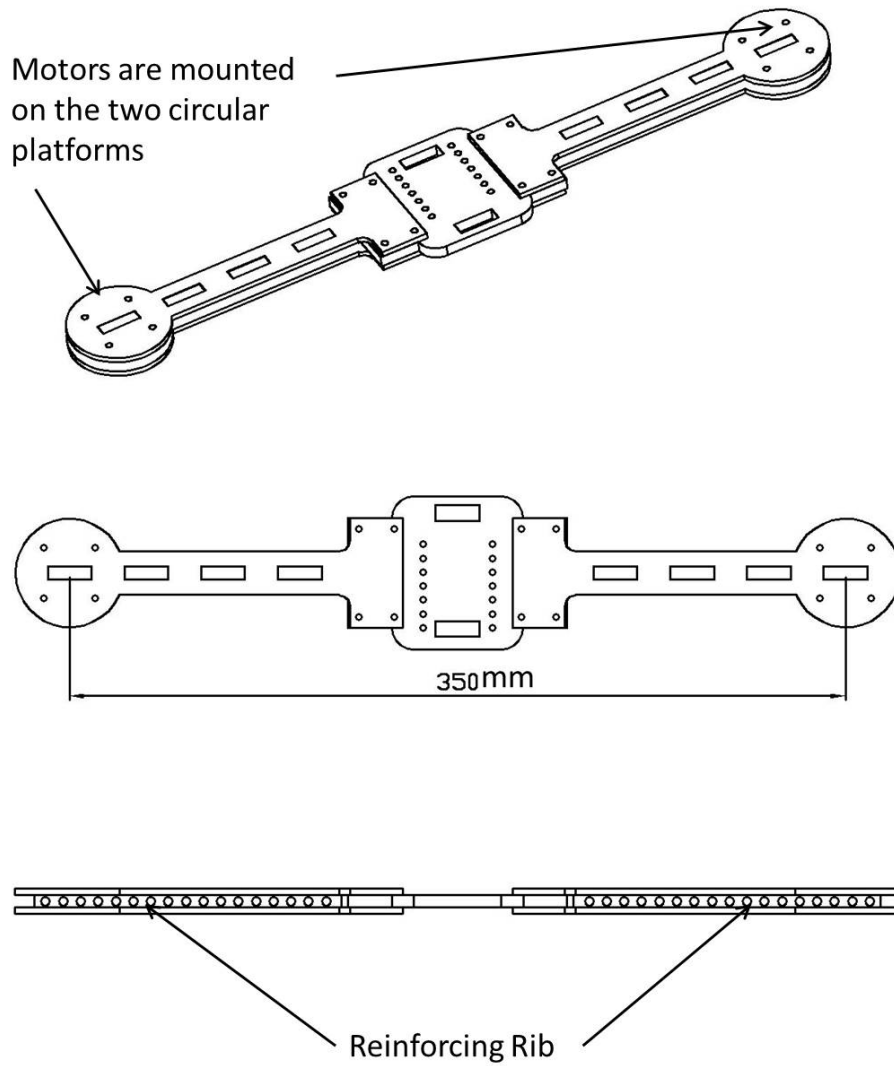
Figure 2.7: Airframe design

A three dimensional model of the MOVA without the robotic arm was constructed and its properties were evaluated using Solidworks® 3D CAD design software (Figure 2.8). The overall mass is 178.91 grams and the moment of inertia taken at the roll axis is 1306.0337 $kg\,mm^2$. The properties will be referenced in the arm design.
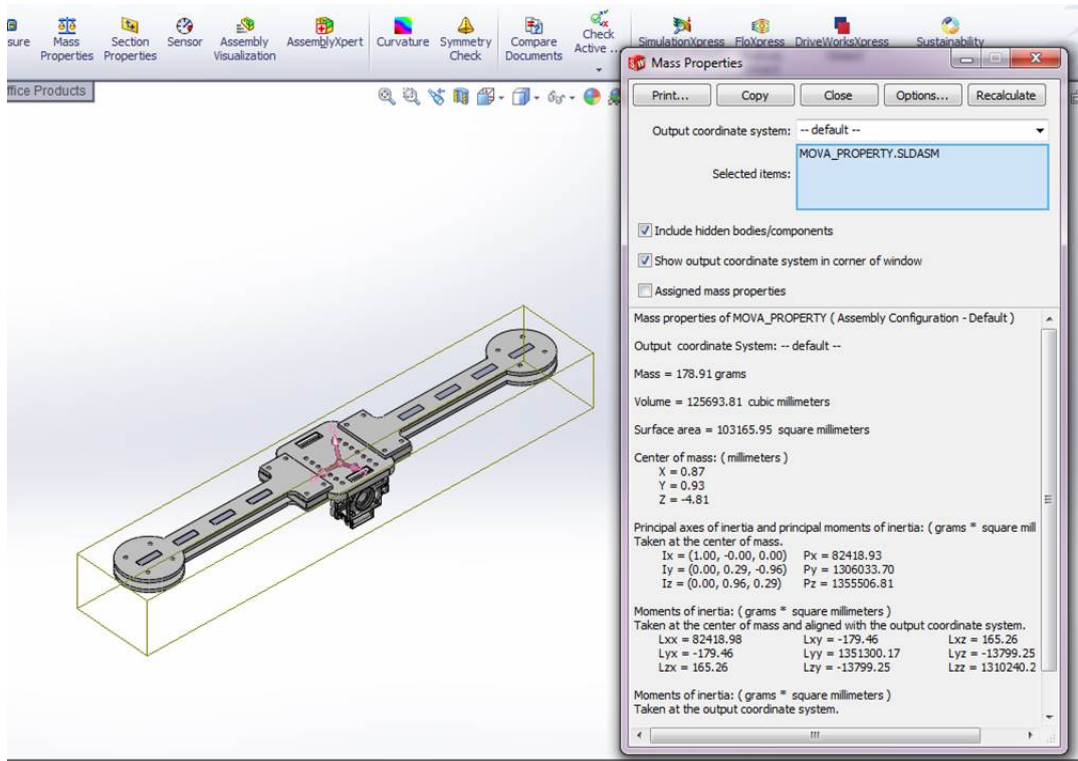
Figure 2.8: Airframe property evaluation

2.4.2 Single-link Robotic Arm Design

The robotic arm is designed as a "pendulum" shape. One of its ends will be attached to the motor on the frame so that the arm can turn like a pendulum to provide the interaction with the VTOL aerial vehicle. To test the MOVA performance under different levels of interaction, the mass and moment of inertia can be changed. The arm consists of three layers. Slots for screws are cut at the middle of each layer such that the middle layer can slide back and forth to adjust the length of the arm (Figure 2.9). The moment of inertia varies as the length changes. The layers can be secured in place by tightening the nuts.

A DC motor [21], is selected to drive the arm. It has an integrated quadrature optical encoder which provides a resolution of 64 counts per revolution. Considering

Figure 2.9: An illustration of Single-link robotic arm structure

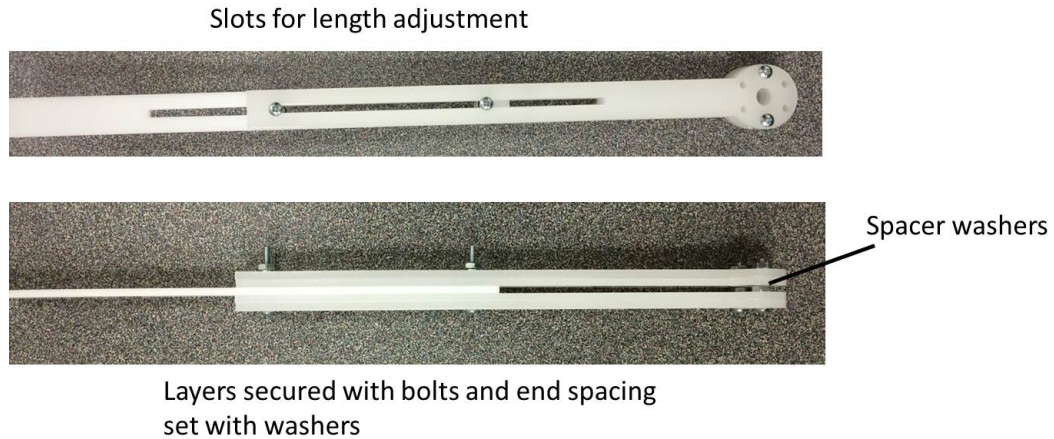its gear ratio, the resolution at the motor output shaft is 1216 counts per revolution, which is 2.72×10^{-4} radian per count. The resolution greatly exceeds that of the position sensor, thus it fulfills the measuring requirements. Including the DC motor, the single-link robotic arm weighs 128 grams. The overall 2D MOVA weighs as 310 gram. Figure 2.10 shows the assembled robotic arm module. The motor specifications can be found in Table 2.9. Note that the rated voltage is 12 V but the motor will be operated in the range 6 V to 12 V. The arm motor specifications will be referenced in Chapter 3.

Rated voltage	Gear ratio	No-load speed	Stall torque at rated voltage	Stall current at rated voltage	Size
12V	19:1	500RPM	0.593N.m	5A	37D x 52L mm
6V	19:1	256RPM	0.297N.m	0.25A	37D x 52L mm

Table 2.9: Specifications of arm motor
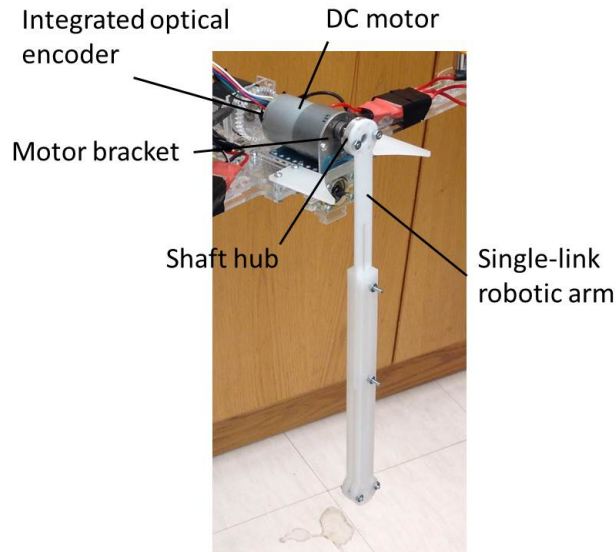
Figure 2.10: Robotic arm and DC motor assembly

2.4.3 Linear Power Amplifier

In order to output a variable voltage to move the DC motor, a programmable power amplifier is needed to connect the Q8 analog output and the actuator of the end-effector. The amplifier model used in the test bed is Techron 5530. It is able to deliver power from DC to 20 KHz under single channel mode. The maximum DC output is 10A at 100V. Calibration is required to perform a unity voltage gain. The wiring of the amplifier can be found in Figure 2.11.

2.5 Propulsion Module Design

2.5.1 Brushless DC Motor

Brushless DC (BLDC) motors are popular motors for model aircraft including quadcopter, due to their large power-to-weight ratio and low cost. Two BLDC motors used in the test bed are the A2212 Brushless Outrunner Motor (Figure 2.12). The

Figure 2.11: The Techron 5530 amplifier was set to operate at mono channel.

motor requires 10 V of input voltage and maximum current is 10 A. It weights 47 grams, with a Kv rating of 1000 RPM/V. The Kv ratings for differ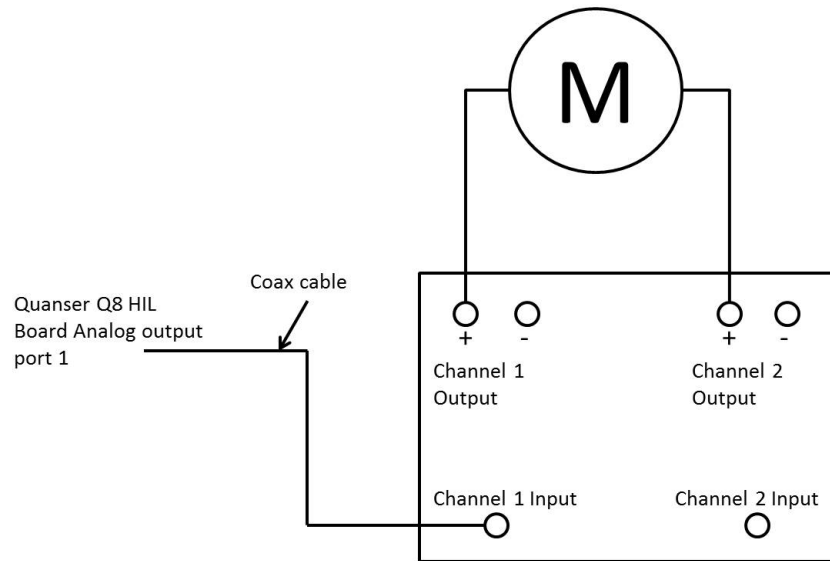ent brands of motors vary from hundreds to thousands and it denotes the number of motor revolutions per minute for every volt of input. A motor with high Kv rating has high maximum speed but low torque. On the contrary, a low Kv rating represents high torque and fast acceleration but low maximum speed. In the two motor test bed, higher torque from each motor is required for take off and to efficiently maneuver the vehicle.

2.5.2   Electronic Speed Controller (ESC)

The brushless electronic speed controller (ESC) provides commutation to turn the brushless motor, by transforming DC power to alternating current to the motor. The ESCs set the desired speed for different motors to achieve flight control by sending pulsating signals of different frequencies. The current rating of the ESC should be larger than that of the brushless motor to prevent a circuit burn out and failure. Given the maximum current of the motor is 10 A, the ESC made by Turnigy is
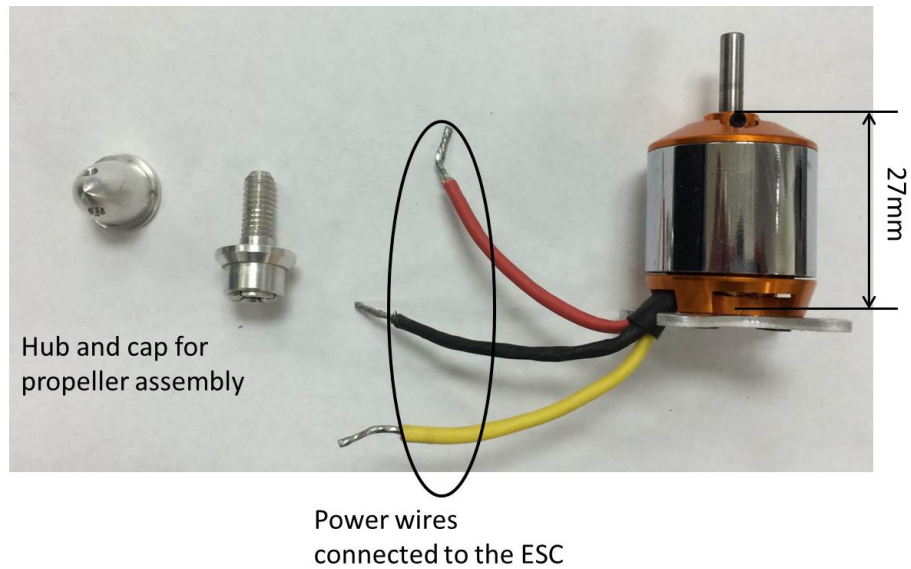
Figure 2.12: An illustration of A2212 BLDC motor parts and dimension

selected, which has a current rating of 30 A.

The ESC cable connections are shown in Figure 2.13a. Three wires on the output side go between the ESC and the motor. Swapping two of them will result in direction reversal of the spin of the motor. On the input side of the ESC, there are power supply wires and standard RC servo interface wires. With a built in battery eliminator circuit (BEC), the ESC can provide power for an RC receiver through the red and black wires (shown in Figure **??**). The white wire in the middle carries the PWM command signal from RC receiver or control board to the ESC. There are no radio controlled units applied to the test bed, and the Q8 control board has independent power supply core, therefore the smaller power supply wires will not be used.

The ESCs each expects a pulse width modulated signal (PWM) (as shown in Figure 2.13b) to drive the motor. The compatible PWM signal must have a PWM period of 20 milliseconds. The duty cycle varies from 1.2 milliseconds to 1.8 milliseconds, resulting in 0% to 100% motor power. The Turnigy ESC was selected

to control the BLDC motor on the 2D MOVA. The Turnigy ESC supports higher PWM frequency up to 500 Hz; compared to the 1000 Hz xPC sampling rate, it is a good match.
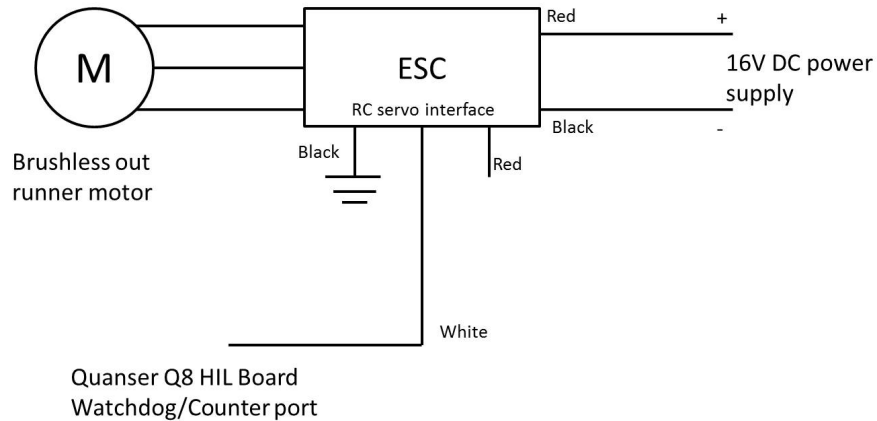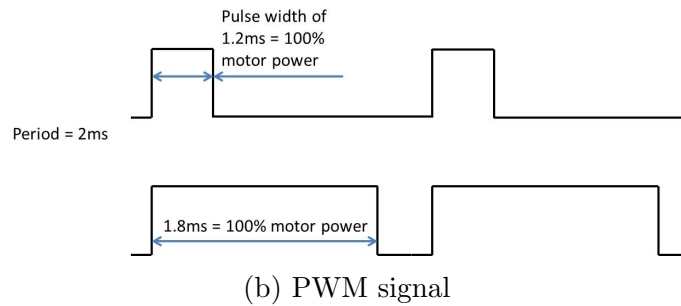

(a) An illustration of ESC wiring

(b) PWM signal

Figure 2.13: Turnigy ESC wiring and PWM signal

2.5.3 Power Supply

The power source for the ESC is a 110V AC to DC power supply with output DC voltage 12V with maximum power of 36 Watts. It provides three DC outputs. The power supply replaces batteries that are normally used in model aircraft and provides stable voltage to the motor.

2.5.4 Propeller Selection

The 2D MOVA uses one clockwise and one counter-clockwise propeller. They spin in different direction to counter balance the torque generated on the yaw axis. Propellers have two key specifications–length and pitch. The length is measured tip to tip while pitch denotes the advancing distance in one revolution. Generally speaking, long length creates high thrust but is slow in response due to the larger inertia, while large pitch provides large acceleration yet may create turbulence. Other factors, such as material, weight, blade number, motor power, with length and pitch together determine the stability and agility of a VTOL.

It is difficult to find an ideal combination of BLDC motor and propeller through computation. As a general rule, a motor with Kv rating of 900-1000 can drive a propeller 10 inches long and 4.5 to 6 inches pitch. For an indoor test bed, stability is the first priority. Small pitch helps to reduce vibration and turbulence that cause the VTOL to wobble when hovering. So the pitch of the propeller is chosen to be 4.5 inches. Considering a large propeller with light weight can produce fast step response, and a soft material improves the MOVA safety, a pair of Maxx Product 10 (length in inch) x 4.5 (pitch in inch) EPP1045, plastic propellers was selected to mount on the motor.

None of the propellers on the market are perfectly balanced. Unbalanced propellers yield considerably large vibration. Such vibration travels through the entire air frame and introduces harmful noise to the onboard sensors and may even damage the motor bearings and parts. Propeller balancing reduces the vibration thus significantly improves the overall system stability and elongates the parts longevity. This was done using a balancer (Figure 2.14). The propeller is installed on the balancer shaft and the blade is aligned horizontally. If it rotates out of the horizontal align-

ment, material removal from the heavy side of the blade is needed. Sandpaper was used to remove the blade material. This step was repeated several times until the propeller rests at the horizontal position.
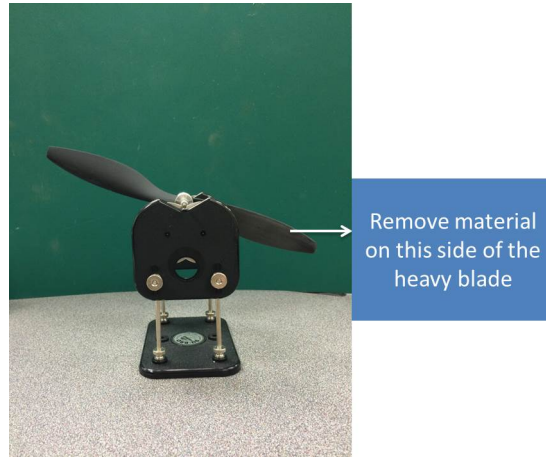

Figure 2.14: Propeller balancer

2.6   Propulsion Module Modeling and Testing

The electronic speed controller (ESC) commands the brushless motor to turn at a speed commanded by sending apply pulse width modulation (PWM) signals with different duty cycles. In order to achieve accurate control, the ESC-motor subsystem must be characterized, two tests were performed. One was used to record the commanding PWM set point and measure the resulting static thrust generated by the motor/propeller. The second was to derive the transfer function of the motor system through measuring its frequency response. By inspecting its dynamic model, the effect of ESC control lag can be evaluated and a rough understanding of the limit frequency of the desired trajectory for the MOVA test bed can be gained.
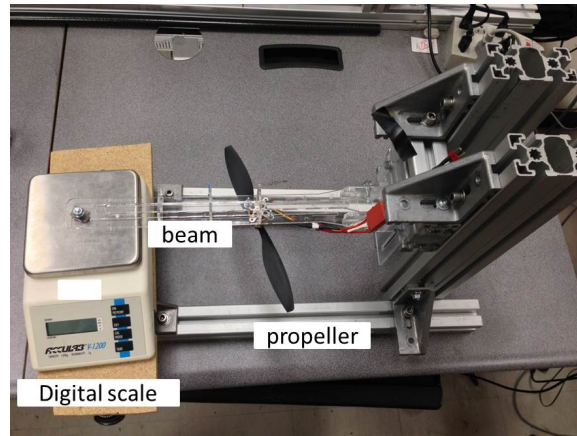
2.6.1 Static Thrust Test

Static thrust is the thrust generated from a stationary motor. As shown in Figure 2.15a, a test bench was constructed to measure the thrust. The beam was made of acrylic plastic and connected to the base through a hinge. The other end of the beam was placed on a digital scale, which had been zeroed before every test. The brushless motor is mounted at the middle of the beam, at a distance l from the hinge, the motor was mounted upside down. A downwards thrust is generated as the motor turns. Through lever principle (Figure 2.15b) the actual thrust can be calculated from the scale reading.

$$F = \frac{fL}{l}. \tag{2.4}$$

Feeding the ESC with different PWM signals, different thrust is generated and recorded on the scale. The test method is to increase PWM set points from 1.2 ms to 1.8 ms with 0.01 ms increments and then to record the thrust data at each set point. After recording several set points a mapping from PWM signal to thrust was formed. The static motor speeds were recorded at the same time using a handheld non-contact laser tachometer from Tester US, model number DT-2234C.

Both of the two motors/propellers were tested using the above method, results data can be found in Appendix (A). Figure 2.16 shows the plot of static thrust versus commanded PWM signal. As can be seen that the thrust and the command is not linear. The reason has to do with the motor efficiency itself and the dynamic of the rotor. A lookup table based on the test result was constructed in Simulink model to linearize it.

(a)
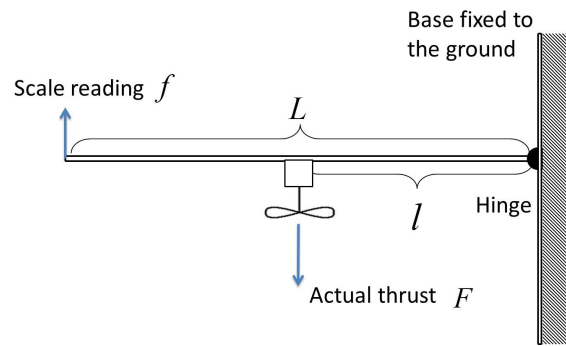
(b)

Figure 2.15: Static thrust test bench

## 2.6.2 Frequency Response Test

The transfer function of the BLDC motor-ESC subsystem is derived through measuring the frequency response of the propulsion module. A speed sensor is constructed using a photo diode to measure the dynamic motor speed.

2.6.2.1 Motor Speed sensor

One of the most popular devices to measure dynamic motor speed is the optical encoder. The usual way to use the encoder is to mount the coding disk to the motor shaft so that the disk will rotate synchronously with the shaft (Figure 2.17a). Motor position is measured by counting the pulses and velocity is derived (Figure 2.17b).

40
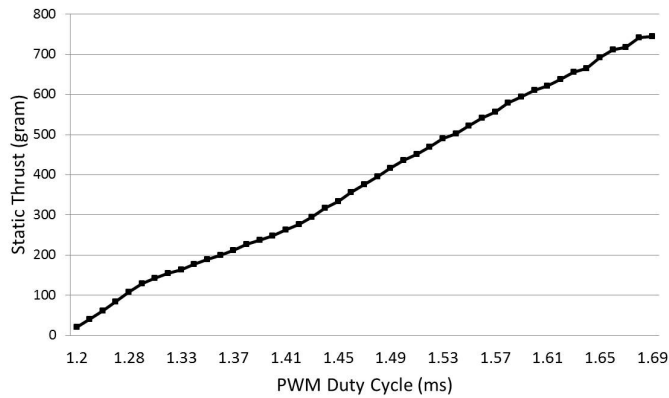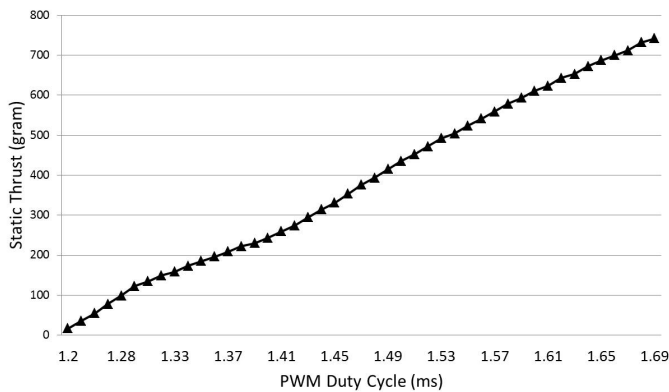
(a) Thrust of Motor A

(b) Thrust of Motor B

Figure 2.16: Static thrust test plot of two motors

However, such assembly configuration is not suitable for the brushless motors used here due to the propeller installation that takes the entire shaft. Alternatively a Hall effect sensor is widely used to detect rotor position in many brushless motors by generating pulses for the rotating magnets. In this case the rotor of the BLDC motor is the external case that has magnets fixed inside. The motor case blocks the internal magnetic field thus renders the switching magnetic pole undetectable by the Hall-effect sensor from outside. Also due to its compact design, there is no way to mount a sensor inside to detect the switching coils.

An encoder-like speed sensor was designed using photo diodes to measure the

41
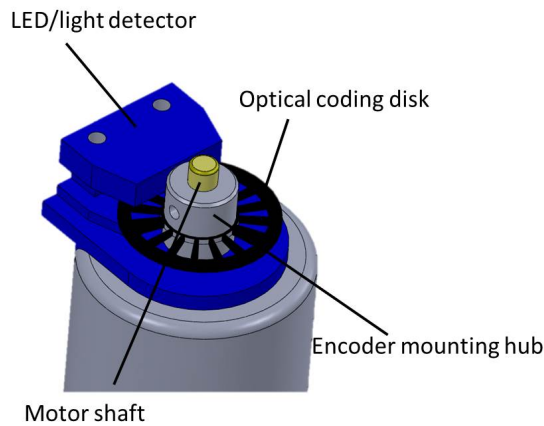
(a) optical encoder coding disk assembly
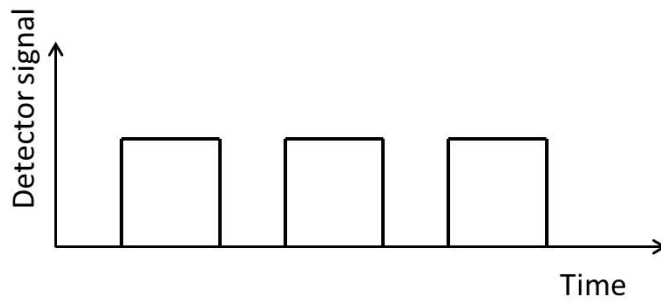
(b) Optical generated pulses

Figure 2.17: Optical encoder

dynamic motor speed. As shown in Figure 2.18, the surface of the case was converted to create alternating absorbtive and reflective surfaces using acrylic glass protective film. In order to suppress the interference of visible light, infrared LED emitters and infrared diodes were used. The LED and photo diode were fixed relative to the motor housing. They are arranged at such an angle that the reflection of the LED from the motor case can be mostly received by the diode. When the motor case spins with the shaft, the level of reflection changes from the diode's aspect.

Variation in the reflection causes the voltage of the diode to change when it is connected in a circuit. The voltage is then compared with a reference voltage in an operational amplifier (Figure 2.19). At the moment a grid is turning past the
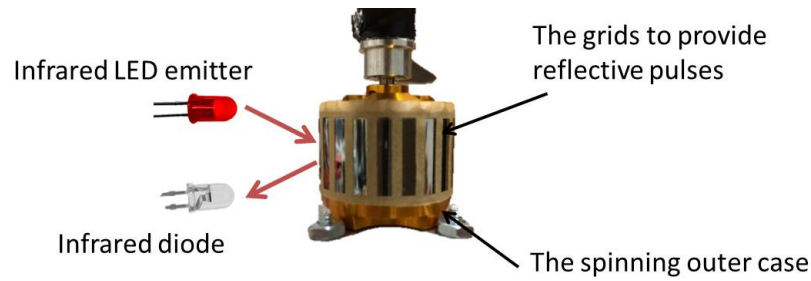
Figure 2.18: Speed sensor configuration

LED, a pulse is generated at the circuit's output when the diode's voltage is higher than the reference voltage. The pulse is sent to the Q8 board's encoder input and the number of pulses is counted in the encoder chip. Just like the encoder's coding disk, the more grids cut on the film the higher the resolution of the sensor. However there is a minimum area required by the diode to generate enough voltage difference to create a change between reflective and non-reflective windows. In the proposed design, twenty windows are cut on the low reflection film.
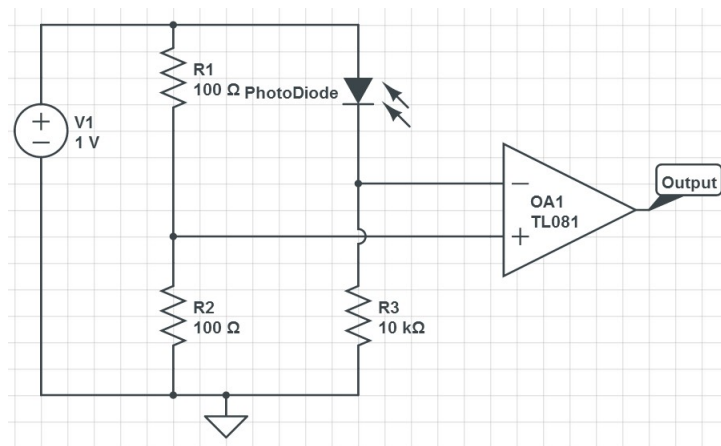

Figure 2.19: infrared diode circuit

2.6.2.2 Frequency Response

The ESC-motor system is assumed to be a first order system with a communication delay of T_d seconds. T_d is selected as 5 milliseconds, and the transfer function is assumed to be

$$G(s) = \frac{1}{Ts+1}e^{-T_d s}. \tag{2.5}$$

After mounted with a propeller, the motor is commanded to track a desired sinusoidal speed with different frequencies. Frequencies were selected from 0.25 Hz to 1 Hz with increments of 0.25, from 1 Hz to 3 Hz with increments of 0.1, and from 3 Hz to 8 Hz with increments of 1. The resulting motor speeds were recorded. As shown in Figure 2.20, the accelerating parts and decelerating parts are not symmetric. This is due to the aerodynamic drag of the propeller and the ESC not applying braking while it commands the motor to slow. The temporal displacement between desired speeds and actual speeds are measured.
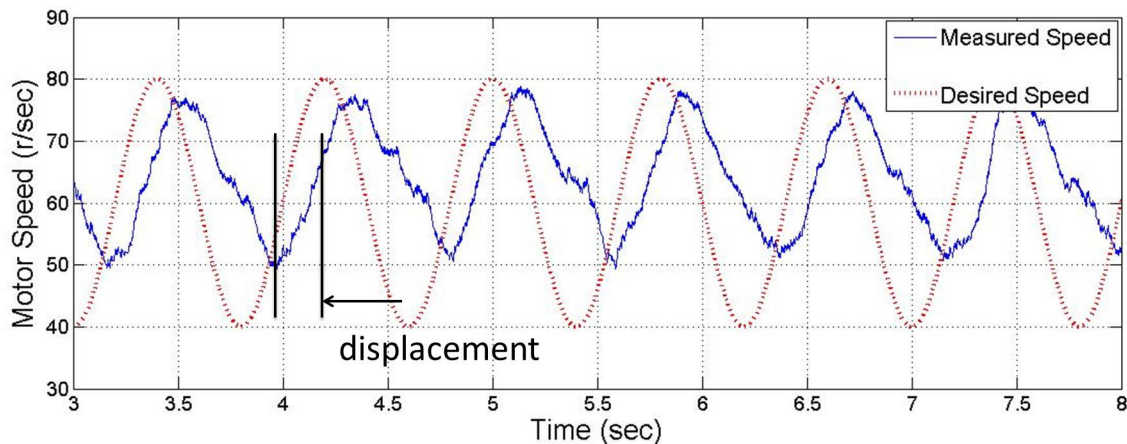

Figure 2.20: Plot of desired speed and actual speed at frequency 0.75 Hz

A bode phase plot is formed by plotting all the measured phase shift data in degrees and the corresponding frequencies in radians/s (Figure 2.21). From the Bode phase plot, T can be estimated as 0.113 seconds. Therefore the ESC-motor system

44

transfer function is identified as:

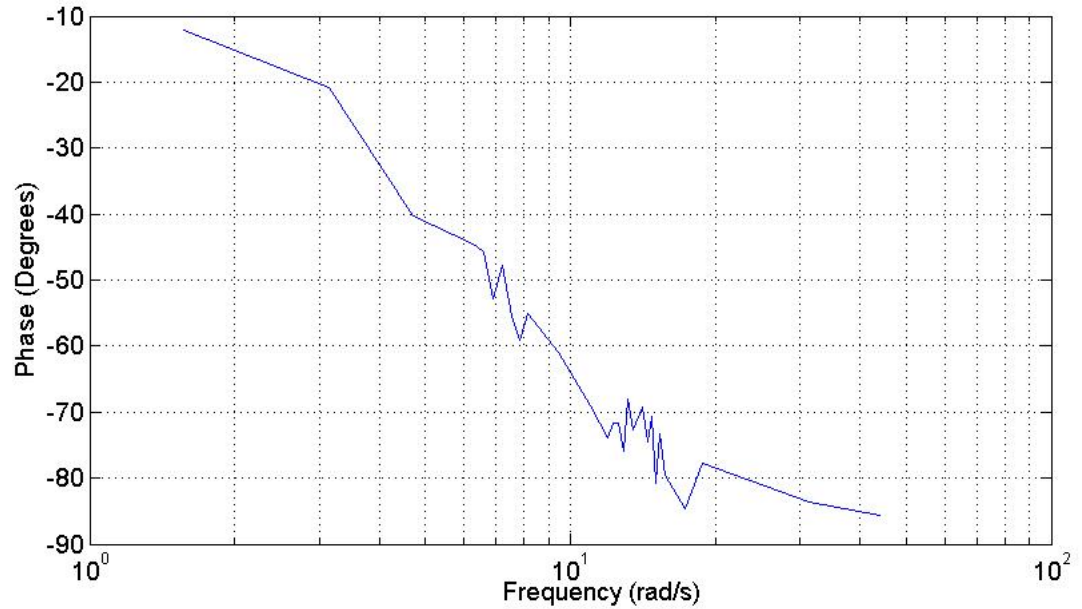$$G(s) = \frac{1}{0.113s + 1} e^{-0.005s}. \tag{2.6}$$

Figure 2.21: Bode phase plot of ESC-motor system

To improve the overall system performance, it is desired for the propulsion module to have a large phase margin. A compensator can partially improve the subsystem frequency response. Based on Equation (2.6), a Phase Lead Compensator (2.22) is designed to reshape the frequency response.

$$G(s) = \frac{s + p_o}{s + p_n} \tag{2.7}$$

As shown in Figure 2.22 the compensator pulls the pole of the uncompensated system further away from the imaginary axis to p_n, resulting in higher phase margin.
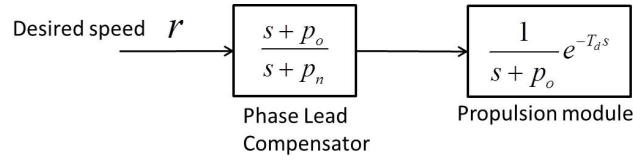
(a) A diagram of the lead compensator
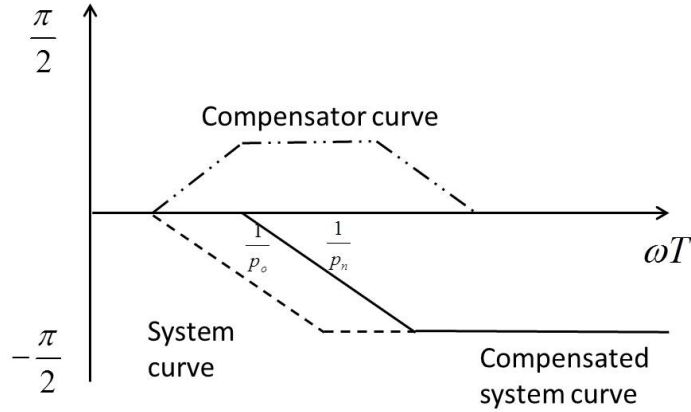
(b) A simplified Bode phase plot that shows how the system frequency curve is reshaped by the compensator

Figure 2.22: An illustration of the Phase Lead Compensator

By reference to the system transfer function, p_o is equal to 9. The lead compensator has increasing gain as frequency increases. Hence the value of p_n must be carefully considered to avoid too much high frequency noise. Through trial and error, p_n=80 was picked.

2.7 Attitude Estimation

2.7.1 Attitude Estimation using Encoder

Attitude control is a basic control objective for all aerial vehicles. The quality of attitude estimation determines the controller performance. In the proposed test bed, the only attitude position is the roll angle. In order to simplify the design process, position feedback through a mechanical method is first studied. With the

constraint of the tether, evaluating the rolling motion of the 2D MOVA can be viewed as measuring the rotary joint where the UAV attaches to the tether. It is desired to use an optical encoder to measure angle, first and second differentiation of the measurement provides an estimate of the angular rates and accelerations.

The roll angle change of the 2D MOVA is very little. Given that the control algorithms are dependent on attitude feedback of high accuracy, an encoder with acceptable resolution is required. Since the encoder will be mounted on-board or fixed with the tether linkage, it will work under the influence of vibration which is produced from the propulsion unit. The encoder should provide reasonable measurements that support the estimation of the velocity and acceleration. After careful consideration, the TRD-S2500 quadrature encoder provided by Koyo was selected. It provides a resolution of 2500 pulses per revolution, requires 5V DC input. The encoder body is 1.5 inches diameter and 1.6 inches depth and weights 42 grams thus is compact enough to put onboard.

2.7.1.1   Gear Design to transmit rotary motion

Due to the limited space on the airframe, the encoder is designed to mount on the tether linkage. As shown in Figure 2.23, a clamp is constructed by two pieces of acrylic plastic to secure the encoder bracket.
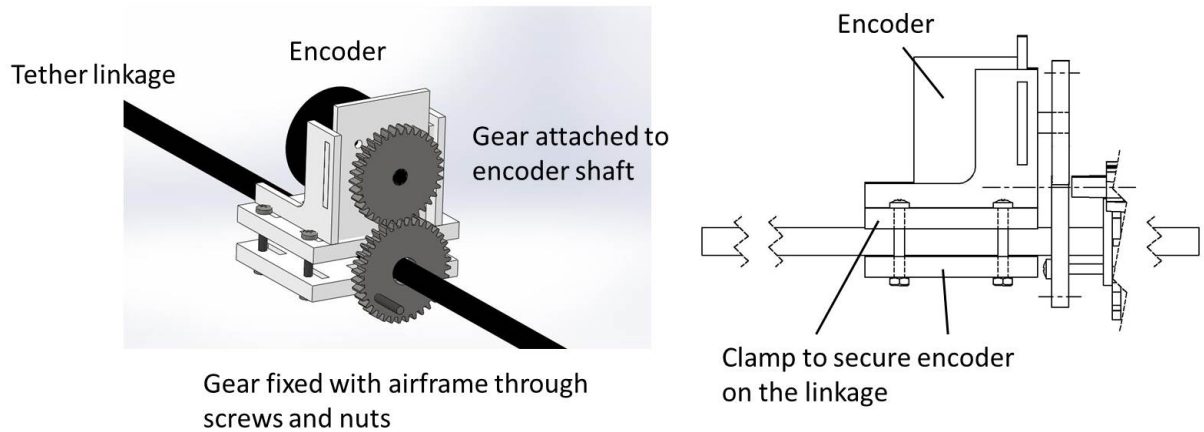
Figure 2.23: The encoder is mounted on a bracket, which is secured on the tether linkage by the clamp.

The motion of the 2D MOVA is transmitted to the encoder through gear engagement, which has a gear ratio of 2:1. The resolution can be evaluated to be

$$\frac{2\pi}{2000} = 0.00314 \text{radian/pulse.} \tag{2.8}$$

All parts built in this section are machined with the laser cutter using acrylic plastic sheets. The detailed dimension and CAD drawing of each part is shown in Appendix B.

2.7.2   Attitude Estimation using PS Eye Camera

The motivation of applying external (off-board) camera feedback is a smaller system weight. By measuring the attitude angle through a camera, the onboard encoder, its supporting brackets, wires and the transmission gears can be removed. Furthermore, the friction generated by gear engagement and displacement of the center of gravity can be avoided, which brings the test bed closer to an ideal planar MOVA.

2.7.2.1 Camera Setup

The sensor of the vision feedback system is required to provide adequate resolution and update rate. A PlayStation®Eye (also referred to as PS Eye) digital camera was selected as the sensor. The PS Eye camera was first designed as a gesture recognition sensor for the PlayStation 3 game console, so that the player can interact with the games by their motions and gestures. The camera has two resolution modes: VGA with a resolution of 640 x 480 pixels, and QVGA (Quarter-VGA), 320 x 240 pixels. The update rate under VGA mode is 75 frames per second, and QVGA 125 frames per second.

The CL Eye Platform Driver software provided by Code Laboratories is used as the PS Eye driver. The CL Driver provides multiple application programming interfaces (API) to allow users to manipulate the camera parameters, such as changing camera resolution, adjusting color modes, controlling the sensor exposure time, etc. Because the CL Driver can only be run on a MS Windows platform, so must the image processing algorithm, the camera is connected to a host laptop and streams the video data through the USB port. Figure 2.24 shows the processing procedure.
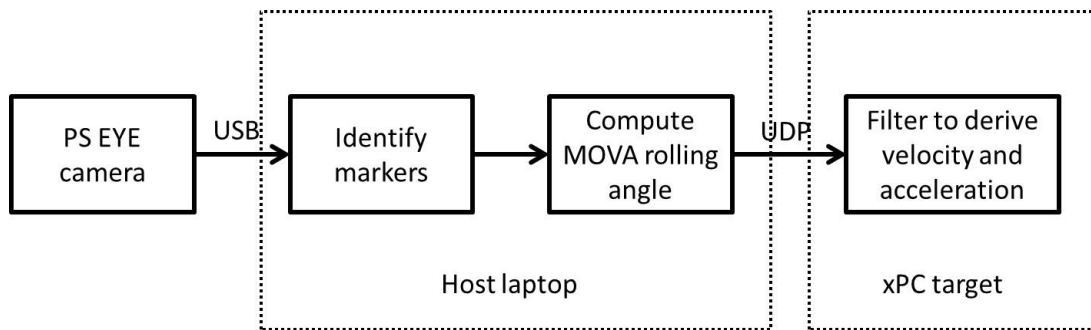

Figure 2.24: A flow chart of using camera to measure MOVA attitude

Two markers to aid in identification are tapped under the BLDC motors, facing in the direction normal to the motion plane. The camera is placed parallel to

the test bed plane (Figure 2.25). The attitude information is can be measured by a single camera. Resolution and MOVA range of motion play the key roles in deciding the distance between camera and the test bed. The distance should be far enough for the camera frame to cover the whole workspace, while keeping the markers clear enough to be identified. Through trial and error, the camera is positioned at 1500mm from the MOVA.
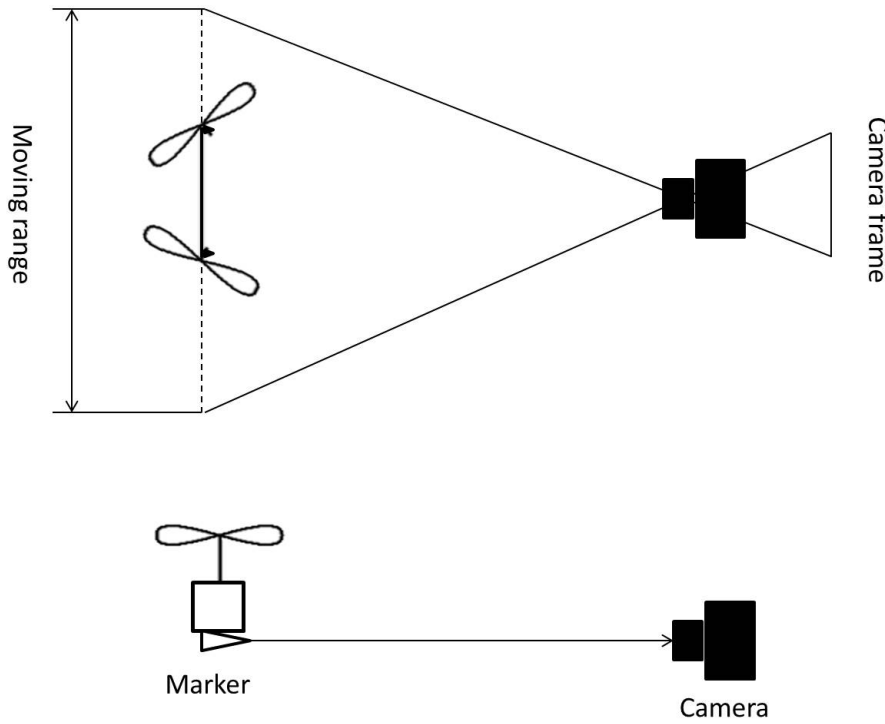

Figure 2.25: An illustration of camera setup

At this distance the physical world that appears in the camera frame is L=1500 mm in length and W=1125 mm in width. In order to guarantee an accurate flight control, the VGA mode (640×480) of PS Eye camera mode is applied. The linear resolution of the camera feedback is found as:

$$\frac{L}{\text{number of pixels along x axis in the frame}} = \frac{1500\text{mm}}{640\text{pixels}} = 2.34\text{mm/pixel}$$

Then the angular resolution can be derived as

$$arctan(\frac{\text{distance resolution}}{\text{length of airframe}}) = arctan(2.34/150) = 0.0156 \text{ radian/pixel}.$$

2.7.2.2 Image Processing Algorithm

The image processing algorithm was implemented in C++ environment. Open Source Computer Vision Library (OpenCV) was used. OpenCV is an open source computer vision and machine learning library. It provides many image processing functions, such as geometric operations, morphology, feature detectors, etc.

The markers are distinguished from the background by their light intensity therefore all the frames are first transformed from RGB to gray scale images. The resulted frames are further transformed to binary images through image segmentation. Erosion and dilation algorithms are called to filter out the noise in the background image.

Two regions of connected pixels (connected components), denoting the rough location of two markers, are identified and labeled. The center of gravity of each region is computed to derive the exact location of the markers with respect to the frame. The actual rotation angle of the VTOL with respect to the ground is evaluated from the angle between the line segments marked by two markers and the x-axis in the frame.

When the algorithm starts, the rotation angle of the first frame, which represents the VTOL original attitude position, is stored. The angles derived from frames afterward are subtracted by the original angle to derive the current attitude position. This way a common start point for encoder and camera measurement is provided, which simplifies the comparison tests elaborated in the following section.
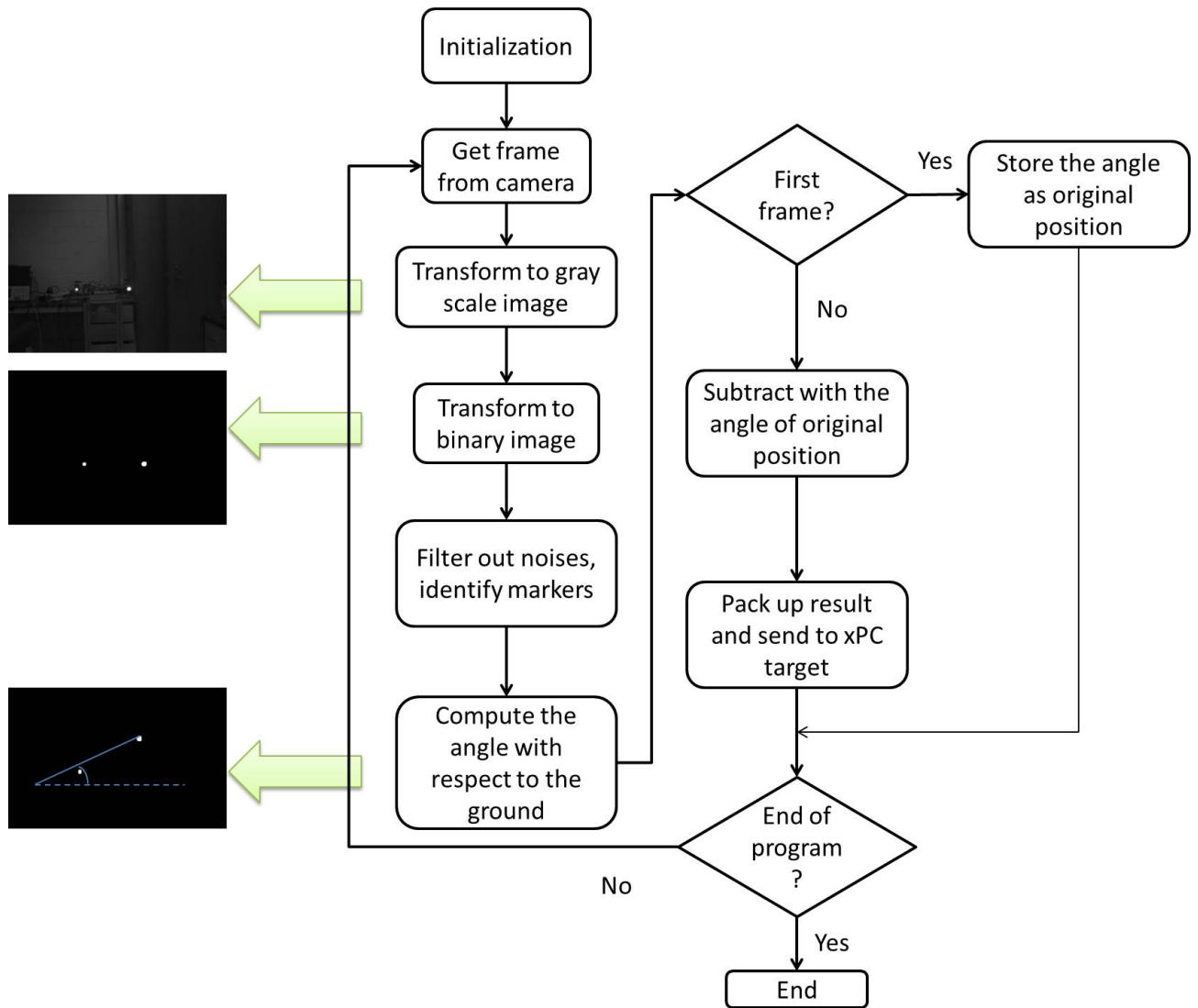
Figure 2.26: A flow chart of the image processing algorithm

2.7.3 Performance Tests and Comparison

The attitude measuring methods based on encoder feedback and based on camera feedback were tested for performance. The test included two parts: 1) observing the attitude estimate by simply moving the VTOL manually with engines off; 2) commanding the PD Controller to track a location set point trajectory based on attitude estimation from camera feedback and then encoder feedback. Since only the attitude

positions of the host 2D VTOL aerial are evaluated and compared, the robotic arm was removed to avoid disturbance. A simple proportional-derivative (PD) controller is constructed to control the 2D VTOL.

2.7.3.1 PD Controller Construction

The dynamic model of the 2D MOVA is constructed by the Newtonian approach as:

$$m\ddot{x} = F sin\theta$$

$$m\ddot{z} + mg = F cos\theta$$

$$J\ddot{\theta} = \tau$$

The system is linearized at the equilibrium point $\theta = 0$. The linearized dynamic function was rewritten in state space matrix form as:

$$\begin{bmatrix} m & 0 & 0 \\ 0 & m & 0 \\ 0 & 0 & J \end{bmatrix} \begin{bmatrix} \ddot{x} \\ \ddot{z} \\ \ddot{\theta} \end{bmatrix} + \begin{bmatrix} 0 \\ mg \\ 0 \end{bmatrix} = \begin{bmatrix} F\theta \\ F \\ \tau \end{bmatrix} \tag{2.9}$$

As the altitude control (motion along z axis) does not involve attitude control after linearization, the z trajectory will not be tested. A constant thrust that equals to the VTOL gravity is applied to maintain an approximately constant altitude. With F held constant, θ can be viewed as the control input for position control

$$\ddot{x} = k\theta_d.$$

Controller computes a desire θ from errors in current position according to

$$\theta_d = k(x_r - x).$$

The attitude control is then achieved by computing the errors of VTOL roll angle and angular rate

$$\ddot{\theta} = \frac{K_p(\theta_d - \theta) + K_d(\dot{\theta}_d - \dot{\theta})}{J}.$$

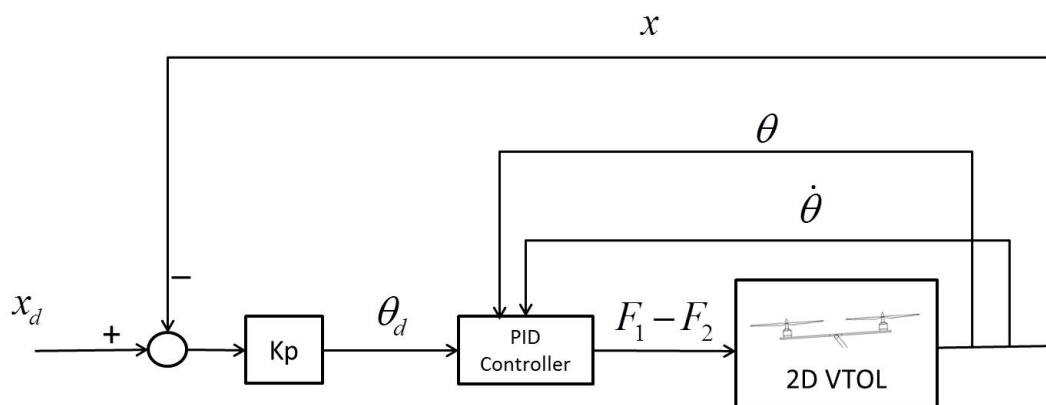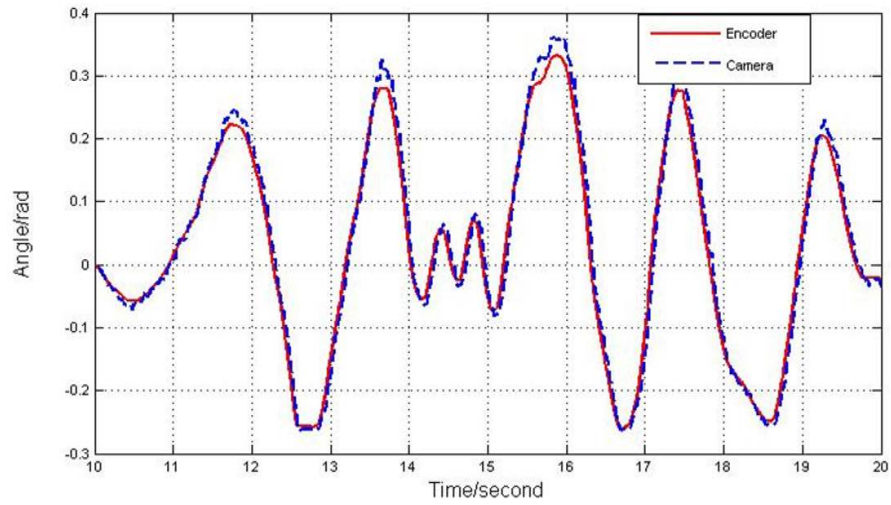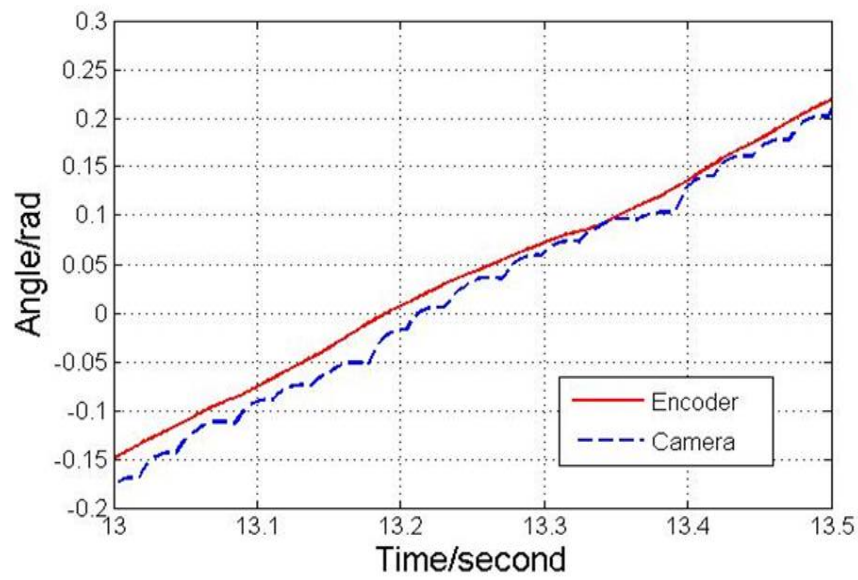Figure 2.27 shows a schematic of the PD controller design.

Figure 2.27: Diagram of the PD Controller.

2.7.3.2 Manually Moving the VTOL

The 2D VTOL was manually moved at angles from roughly +0.3 radian to -0.3 radian at different velocities. The results are shown in Figure 2.28.

(a) Encoder and camera feedback comparison

(b) A zoom in the angle measuring comparison

Figure 2.28: Roll angle measurement of encoder and camera feedback from manual test
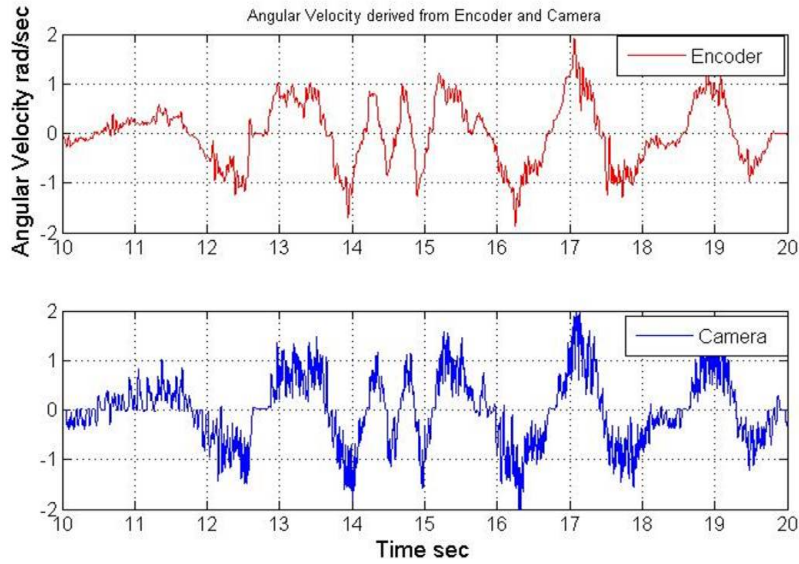
Figure 2.29: A comparison of derived velocity evaluation between encoder feedback and camera feedback

Close inspection of Figure 2.28 reveals that the feedback from camera has around 20 ms delay compared to the encoder feedback. The latency is speculated to include the frame update, computational time for the host PC and the data lost during transmitting to the target PC. Figure 2.29 also demonstrates similar performances on velocity estimation, while the encoder is relatively smoother than the camera.

2.7.3.3 Set Point Trajectory

The set point is set at 0 mm. The 2D VTOL is commanded to stay at the origin in the plane. The controller gain is set to k=1.3, k_p=10.2 and k_d=2.6. Results are shown in Figure 2.30. The steady state errors of the system based on encoder feedback are less than 0.08 m, while the steady error of the system based on camera varies dramatically from +0.25 m to -0.43 m.
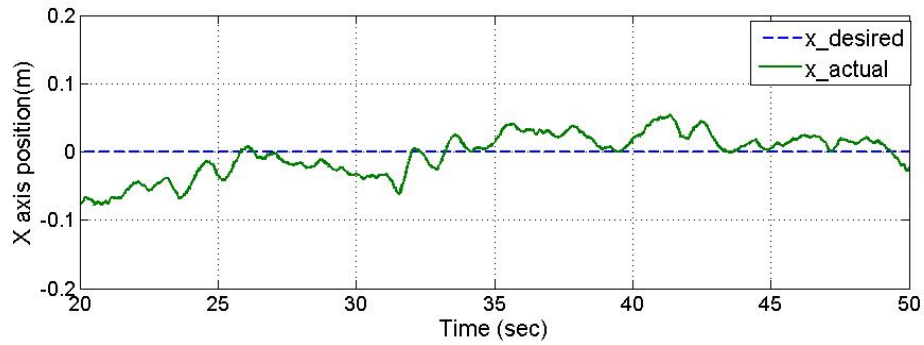
(a) attitude measurement based on encoder feedback
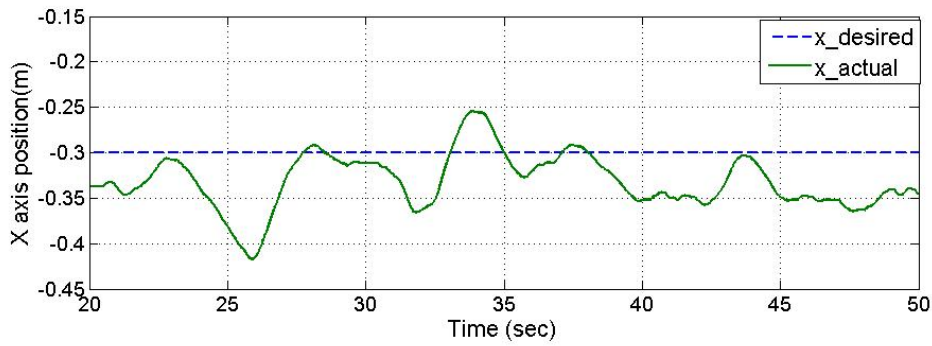
(b) attitude measurement based on camera feedback

Figure 2.30: Comparison of controller position stabilization ability

2.7.4 Conclusion

Using camera to measure attitude angle can improve the overall mechanical construction by removing extra onboard devices, and provide slightly better resolution compared to the encoder. On the other hand, the proceeding section shows that encoder provides better feedback, in terms of response time and noise level. The controller based on encoder feedback also has better performance at tracking a set point location. Therefore the encoder will be selected as the sensor for attitude

estimation of the MOVA.

2.8   Summary

Each module was assembled and the planar test bed was constructed. An exam was performed to validate the system requirements as shown in Table 2.10. The results show that the constructed test bed has met the design requirements.

Module	Requirements	System parameters	Requirement filled
Propulsion module	Maximum thrust is twice of the total weight	1. System total weight is 0.62 Kg. 2. Maximum thrust for each motor is 0.72 Kg and 0.73 Kg respectively. Total thrust is 1.45 Kg;	Yes
Position measurement	5 mm resolution	3.925mm/count (Equation 2.3)	Yes
Attittude estimation	0.02 radian resolution	0.00314 radian/pulse (Equation 2.8)	Yes

Table 2.10: Design requirements checklist

Chapter 3

Experiments and Results

The implementation and testing of the 2D MOVA controller by Xu *et al.*[12][14] on the test bed (shown in Figure 3.1) is described in this chapter. The proposed controller was verified through a series of experiments. The derivation of the 2D MOVA dynamics applying the virtual manipulator method and a nonlinear controller design in Xu's paper is briefly discussed in the first section, along with a description of a separate control strategy (referred to as the Separate Controller), which controls the VTOL and the manipulator separately. The VTOL control is constructed by removing the coupling compensation for the arm-UAV interaction in the MOVA unified controller. The arm is controlled using a PD control. This will serve as the "naive" control strategy reference for comparison to the unified 2D MOVA control. Controller implementations were conducted and experiments were performed to demonstrate the two controllers. Results are presented at the end of the chapter that suggest the potential advantage of the MOVA unified controller over the Separate Controller. The work done here supports the theoretical developments in Peng Xu's dissertation [14], results in the form of plots are shared with Xu's dissertation [14] and the controller described in Section 3.1.1 is an abridged version of the work in [14]. Part of this
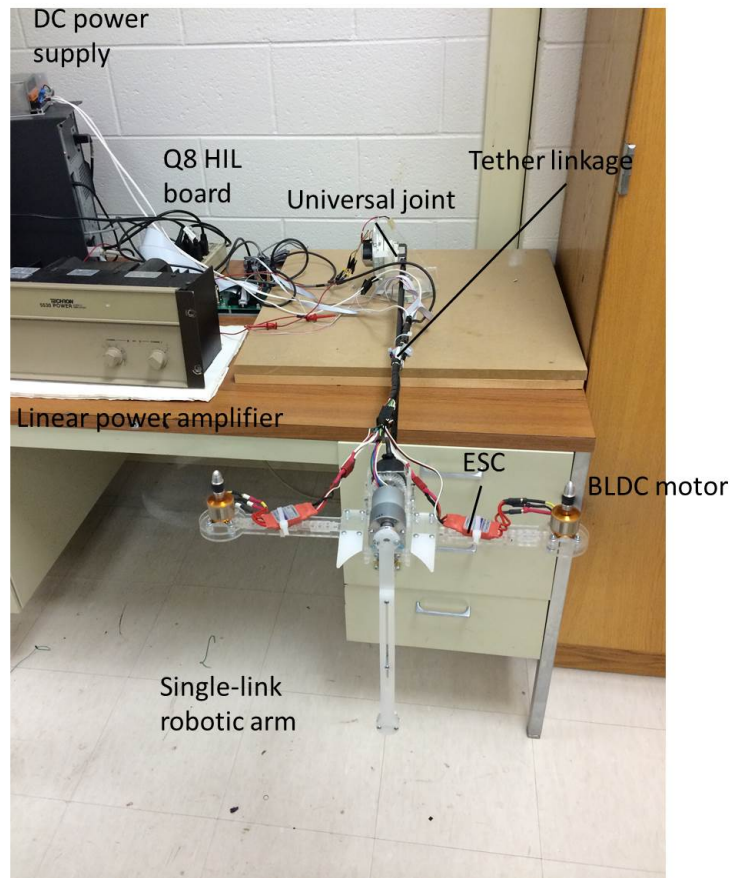
collaboration is a conference paper [12].

Figure 3.1: 2D planar test bed

3.1 Control Strategies and Implementation

Table 3.1 lists the notation definitions used to describe the MOVA system. The notations are defined in [12], and will be used in the following sections describing the MOVA controller.

Symbol	Description
m_0	mass of the VTOL aircraft
J_0	moment of inertia of the VTOL aircraft
m_1	mass of the single manipulator link
J_1	moment of inertia of the dummy robotic arm about its rotation axis
m_T	The total mass of the VTOL aircraft and the manipulator
l_1	length of the dummy robotic arm
p_e	vector of coordinates of the end-effector
θ_0	attitude angle of the VTOL aircraft
θ_1	angle between the VTOL and the arm
θ_{01}	short notation of $\theta_0 + \theta_1$
F	body-fixed thrust force generated by the VTOL aircraft
τ_0	external torque on the body of the VTOL aircraft
τ_1	torque driving the single-link manipulator

Table 3.1: Notation description

3.1.1 MOVA Dynamics Derivation and Control Design

3.1.1.1 Dynamics Derivation

The MOVA dynamics derivation in this section involves two key concepts–the virtual ground and the virtual manipulator. The virtual ground represents the center of mass of the whole system. The coordinate of the virtual ground in the inertia frame can be found for the planar MOVA case as

$$
\begin{aligned}
p_{vg} &= \sum_{i=0}^{N} m_i p_i \\
&= \frac{1}{m_T}(m_0 p_0 + m_1 p_1) \\
&= p_0 + \frac{l_1 m_1}{2 m_T}
\begin{bmatrix}
cos\theta_{01} \\
sin\theta_{01}
\end{bmatrix}.
\end{aligned}
\tag{3.1}
$$

The virtual manipulator can be viewed as series of carefully chosen vectors that start from the virtual ground and end at the exact same end-effector position and with same orientation of the real manipulator. One advantage of the virtual ground and the virtual manipulator over conventional kinematic methods, which starts from the VTOL body to describe the position of end-effector, is that they are immune to the internal torque and force and thus can be viewed as two separate systems. Following the derivation steps, the position of the end-effector can be written as:

$$p_e = p_{vg} + \frac{l_1(m_T + m_0)}{2m_T} \begin{bmatrix} cos\theta_{01} \\ sin\theta_{01} \end{bmatrix} \tag{3.2}$$

and

$$
\begin{aligned}
p_e &= p_{vg} + V_1 + V_2 \\
&= p_{vg} + \frac{l_1(m_T + m_0)}{2m_T} \begin{bmatrix} cos\theta_{01} \\ sin\theta_{01} \end{bmatrix}.
\end{aligned} \tag{3.3}
$$

The detailed derivation process of the virtual ground and virtual manipulator can be found in [14].

The dynamics of MOVA system are derived though a Lagrangian approach, and put into the form

$$M(q)\ddot{q} + C(q, \dot{q})\dot{q} + G(q) = \tau. \tag{3.4}$$

The complete matrices of Equation (3.4) are given by:

$$
M = \begin{bmatrix}
m_T & 0 & -\frac{1}{2}l_1 m_1 sin\theta_{01} & -\frac{1}{2}l_1 m_1 sin\theta_{01} \\
0 & m_T & \frac{1}{2}l_1 m_1 cos\theta_{01} & \frac{1}{2}l_1 m_1 cos\theta_{01} \\
-\frac{1}{2}l_1 m_1 sin\theta_{01} & \frac{1}{2}l_1 m_1 cos\theta_{01} & J_0 + J_1 + \frac{l_1^2 m_1}{4} & J_1 + \frac{l_1^2 m_1}{4} \\
-\frac{1}{2}l_1 m_1 sin\theta_{01} & \frac{1}{2}l_1 m_1 cos\theta_{01} & J_1 + \frac{l_1^2 m_1}{4} & J_1 + \frac{l_1^2 m_1}{4}
\end{bmatrix},
\tag{3.5}
$$

$$
C = \begin{bmatrix}
0 & 0 & -\frac{1}{2}l_1 m_1 cos\theta_{01}\dot{\theta}_{01} & -\frac{1}{2}l_1 m_1 cos\theta_{01}\dot{\theta}_{01} \\
0 & 0 & -\frac{1}{2}l_1 m_1 sin\theta_{01}\dot{\theta}_{01} & -\frac{1}{2}l_1 m_1 sin\theta_{01}\dot{\theta}_{01} \\
0 & 0 & 0 & 0 \\
0 & 0 & 0 & 0
\end{bmatrix},
\tag{3.6}
$$

$$
G = \begin{bmatrix} 0 & m_T g & \frac{1}{2}l_1 m_1 cos\theta_{01} g & \frac{1}{2}l_1 m_1 cos\theta_{01} g \end{bmatrix}^T,
\tag{3.7}
$$

$$
\tau = \begin{bmatrix} -F sin\theta_0 & F cos\theta_0 & \tau_0 & \tau_1 \end{bmatrix}^T.
\tag{3.8}
$$

The dynamic equation clearly shows the off-diagonal terms in $M(q)$ and $C(q, \dot{q})$, which represent the interaction between the onboard manipulator and the VTOL. By applying the virtual manipulator method, the dynamics equation can be rewritten in a more concise form where the virtual ground and the virtual manipulator can be viewed as two separate systems and to facilitate the control design. The decoupled dynamics equation can be found by:

$$
m_T \ddot{p}_{vg} + \begin{bmatrix} 0 \\ m_T g \end{bmatrix} = \begin{bmatrix} -F sin\theta_0 \\ F cos\theta_0 \end{bmatrix},
\tag{3.9}
$$

$$J_0\ddot{\theta}_0 = \tau_0 - \tau_1, \tag{3.10}$$

and

$$\bar{J}_1\ddot{\theta}_{01} = \tau_1 - \xi_1 F, \tag{3.11}$$

where $\bar{J}_1 = J_1 + \dfrac{l_1 m_0 m_1}{4 m_T}$ and $\xi_1 = \dfrac{l_1 m_1}{2 m_T} cos\theta_1$.

3.1.1.2 Control Design

The objective is to design a controller to follow the desired end-effector trajectory $p_{er}(t)$ and $\theta_{er}(t)$. The subscript "r"" denotes a reference version of the variable. By adopting back-stepping technique, a Lyapunov-based nonlinear controller can be derived. The design process can be divided into two parts: virtual ground control design, forcing the virtual ground position p_{vg} to track the desired position p_{vgr}; and virtual manipulator design, directing the end-effector angle θ_{e01} to converge to a reference angle θ_{e01r}

Virtual ground control. A filtered tracking error is first defined as

$$r = e_v + \alpha e_p + \delta, \tag{3.12}$$

where $\alpha \in R^+$ and $\delta = [0, \delta_2]^T$ are control gains. e_v and e_p are filtered tracking errors which are given by

$$e_p = R^T(p_{vg} - p_{vgr}), \tag{3.13}$$

and

$$e_v = R^T(\dot{p}_{vg} - \dot{p}_{vgr}), \tag{3.14}$$

64

R transforms a vector in the inertial frame into VTOL body frame

$$R = \begin{bmatrix} cos\theta_0 & -sin\theta_0 \\ sin\theta_0 & cos\theta_0 \end{bmatrix}, \tag{3.15}$$

$\dot{r}$ can be found by taking time derivative of Equation (3.12). The equation for the r-dynamics clearly shows the control input

$$\dot{r} = S(\omega)r + \alpha e_v - R^T(\ddot{p}_{vgr} + g_v) + \begin{bmatrix} -\delta_2 & 0 \\ 0 & m_T^{-1} \end{bmatrix} \cdot \begin{bmatrix} \omega \\ F \end{bmatrix} \tag{3.16}$$

$$= S(\omega)r + \xi_2 + B_\mu\mu,$$

The above equation is then organized in a more concise form

$$\dot{r} = S(\omega)r + \xi_2 + B_\mu\mu, \tag{3.17}$$

where $\xi_2 = \alpha e_v - R^T(\ddot{p}_{vgr} + g_v)$ and

$$B_\mu = \begin{bmatrix} -\delta_2 & 0 \\ 0 & m_T^{-1} \end{bmatrix}, \text{and } \mu = \begin{bmatrix} \omega \\ F \end{bmatrix}, \tag{3.18}$$

Among the two control inputs, F can be directly controlled by motor thrust, while ω is the output of the θ_0 dynamics. A typical back-stepping technique is applied by injecting a tracking error in Equation (3.17) to yield

$$\dot{r} = S(\omega)r + \xi_2 + B_\mu(\mu_d + \mu_e), \tag{3.19}$$

where

$$\mu_e = \begin{bmatrix} \omega_e \\ F_e \end{bmatrix} = \mu - \mu_d = \begin{bmatrix} \omega - \omega_d \\ F - F_d \end{bmatrix}. \tag{3.20}$$

To regulate r, μ_d is designed as

$$\mu_d = \begin{bmatrix} \omega_d \\ F_d \end{bmatrix} = B_\mu^{-1}(-k_r r - \xi_2 - e_p). \tag{3.21}$$

The control inputs should push the tracking errors to approach 0. It is clear that

$$F = F_d = \begin{bmatrix} 0 & 1 \end{bmatrix} \mu_d. \tag{3.22}$$

While the dynamics of θ_0 is controlled by the net torque applied on VTOL τ_n, which equals to $\tau_0 - \tau_1$, as shown in Equation (3.23)

$$\begin{aligned} J_0 \dot{\omega}_e &= J_0 \ddot{\theta}_0 - \begin{bmatrix} J_0 & 0 \end{bmatrix} \dot{\mu}_d \\ &= \tau_n - \begin{bmatrix} J_0 & 0 \end{bmatrix} \dot{\mu}_d. \end{aligned} \tag{3.23}$$

τ_n is revealed by referencing the Lyapunov stability analysis [15] as

$$\tau_n = -k_\omega J_0 \omega_e + \begin{bmatrix} J_0 & 0 \end{bmatrix} \dot{\mu}_d + \begin{bmatrix} \delta_2 & 0 \end{bmatrix} r. \tag{3.24}$$

End-effector orientation control. Similar to the virtual ground control, a filtered orientation tracking error is formulated as

$$r_2 = \dot{e}_{01} + \beta e_{01} \tag{3.25}$$

where β is the control gain and e_{01} is the error between the actual end-effector orien-

66

tation and the reference orientation, which can be expressed as

$$e_{01} = \theta_{01} - \theta_{01r} \tag{3.26}$$

and

$$\dot{e}_{01} = \dot{\theta}_{01} - \dot{\theta}_{01r}. \tag{3.27}$$

The control input of θ_{01}, τ_1 can be introduced into the tracking error r_2 dynamics by taking time derivative of Equation (3.25) and multiplying $\bar{J}_1$ on both side of the equation

$$\begin{aligned}
\bar{J}_1 \dot{r}_2 &= \bar{J}_1 \ddot{\theta}_{01r} + \bar{J}_1 \beta \dot{e}_{01} \\
&= \tau_1 - \xi_1 F - \bar{J}_1(\ddot{\theta}_{01r} - \beta \dot{e}_{01}),
\end{aligned} \tag{3.28}$$

τ_1 is then specified as

$$\tau_1 = -k_2 \bar{J}_1 r_2 + \xi_1 F + \bar{J}_1(\ddot{\theta}_{01r} - \beta \dot{e}_{01} - e_{01}). \tag{3.29}$$

The external torque applied on the VTOL is revealed to be the sum of τ_n and τ_1

$$\tau_0 = \tau_n + \tau_1, \tag{3.30}$$

At this the point, three control inputs to the planar MOVA system have been specified in Equation (3.22), (3.29) and (3.30).

3.1.2 Separate Control Strategy

The Separate Controller has two separate parts–VTOL control and end-effector control. The VTOL control strategy is constructed following the exact same design

steps as the virtual ground control of the planar MOVA, but based solely on the dynamics of a planar VTOL (Equation (2.9)). Simply put, replace the virtual ground coordinate and reference virtual ground trajectory everywhere in the MOVA dynamics with the VTOL body coordinate and the reference VTOL body trajectory. The external thrust input can be found by Equation (3.22), replacing the reference virtual ground acceleration $\ddot{p}_{vgr}$ with the reference VTOL body acceleration $\ddot{p}_{0r}$ in μ_d. The modified μ_d is written as

$$\mu_d = \begin{bmatrix} \omega_d \\ F_d \end{bmatrix} = B_\mu^{-1}(R^T g_v + \ddot{p}_{0r} - \alpha e_v - ep - k_r r). \tag{3.31}$$

The control input thrust F is

$$F = \begin{bmatrix} 0 & 1 \end{bmatrix} \begin{bmatrix} \omega_d \\ F_d \end{bmatrix} = B_\mu^{-1}(R^T g_v + \ddot{p}_{0r} - \alpha e_v - ep - k_r r). \tag{3.32}$$

Same process applies for finding the external torque on the VTOL τ

$$\tau = -k_\omega J_0 \omega_{0e} + \begin{bmatrix} J_0 & 0 \end{bmatrix} \dot{\mu}_{0d} + \begin{bmatrix} \delta_2 & 0 \end{bmatrix} r_0, \tag{3.33}$$

where $\omega_{0e}, \dot{\mu}_{0d}$ and r_0 are the VTOL body version of the corresponding variables.

The end-effector control applies a typical PD controller, which tracks desired rotation angles with respect to the VTOL. Note that the desired inputs from the user are the end-effector position P_{er} and the end-effector direction θ_{er}, with respect to the inertial frame. While the input to the separate controller is the position and attitude angle, which are denoted as p_r and θ_{0r}. Therefore the input coordinate to the separate system must first be transformed to a VTOL coordinate before being

68

sent to the Separate Controller.

3.1.3 Controller Implementation

Both of the systems were implemented through Simulink models and executed by an xPC Target workstation through the Q8 HIL board. The Q8 board was set at a sampling rate of 100 Hz. Note that the MOVA control input to the on-board manipulator is torque computed by the control algorithm while the DC motor that drives the manipulator requires voltage input. The desired voltage output can be computed by referencing to the DC motor voltage equation

$$V_m = E_b + R_m I_a. \tag{3.34}$$

The notation definitions in the equations can be found in Table 3.2. E_b and I_a can be derived from

$$E_b = k_e \dot{theta}_1, \tag{3.35}$$

and

$$I_a = \frac{\tau_1}{k_T}, \tag{3.36}$$

where k_e is the motor back emf constant and k_T is the torque constant. An equation involving the manipulator angular speed and input voltage is derived by injecting Equations (3.35) and (3.36) into Equation (3.34) to yield

$$V_m = k_e \dot{\theta}_1 + R_m \frac{\tau_1}{k_T}. \tag{3.37}$$

Values in Table 2.9 were assigned to the corresponding variables in Equation (3.37) and computed for $k_e = 0.07$ Vs/rad and $R_m = 2.4\Omega$. Note that $k_T = \dfrac{k_e}{2\pi} = 0.01$

Parameters	Definition
v_m	Motor input voltage (V)
E_b	Motor back emf
R_m	Motor resistance
I_a	Motor armature current

Table 3.2: Notations definition in manipulator motor voltage derivation

Nm/A. The desired voltage output to the motor can be derived by substituting into Equation (3.37) with values derived and the computed torque from control algorithm. The values for the VTOL parameters can be found in Table 3.3. It is worth pointing out that the mass and moment of inertia of the VTOL aircraft and the single link robotic arm are comparable.

Parameters	Value
m_0	0.61 Kg
m_1	0.07 Kg
l_1	0.3 m
J_0	15.9 $\mathrm{kg\,mm}^2$
J_1	3250 $\mathrm{kg\,mm}^2$
g	9.8 $\mathrm{kg/mm}^2$

Table 3.3: System parameter value

Table 3.4 lists the control gains used in both systems. Note that the same control gains are used in the virtual ground control of the MOVA system and the Separate Controller controlling the VTOL to ensure the validity of the comparison. The translational displacements were computed from the optical encoders of Tohoku motors multiplied by l_1. θ_0 was derived by multiplying the measurement of TRD-S2500 encoder with the gear ratio 2.

Gains	Value
k_r	0.08
k_ω	0.06
α	1
δ_2	1.1
β	13
k_2	94
P (propotional gain)	10
D (derivative gain)	0.1

Table 3.4: Value of control gains

3.2 Experiments and Results

In order to evaluate the planar MOVA controller, three experiments were conducted, and the performance compared with the Separate Controller. The first experiment was designed to test the hovering stability of the MOVA. The system initial states were set to $\begin{bmatrix} x_e & z_e & \theta_{01} \end{bmatrix}^T = \begin{bmatrix} 0 & -0.3 & -\frac{\pi}{2} \end{bmatrix}^T$. Specifically the initial attitude of VTOL and the initial attitude of manipulator were $\theta_0 = 0$ and $\theta_1 = -\frac{pi}{2}$, respectively. The desired trajectory was to hover at the same location and manipulate orientation. The MOVA results are compared with the results of the Separate Controller in Figure 3.2. The system was hand held until the motors reach the desired speed because the differential response time of the two motors may lead to sudden attitude change when taking off. The data period displayed was carefully selected to present the largest error that appeared during the whole testing cycle. The same rule applies for the other tests.
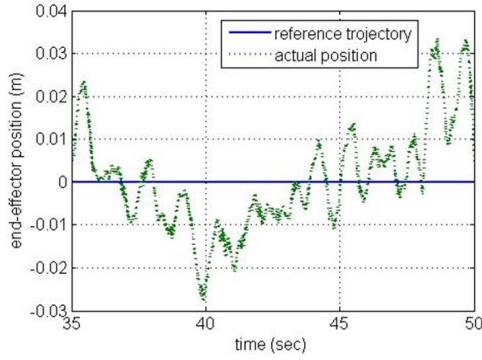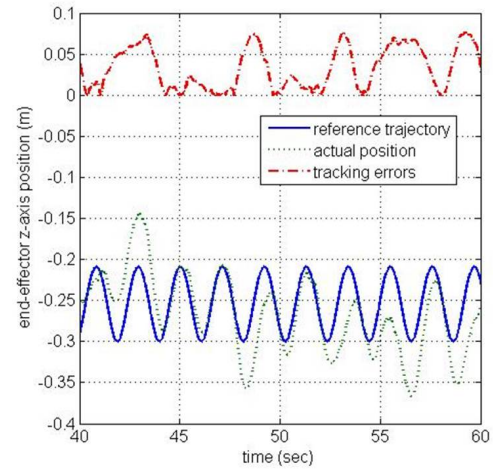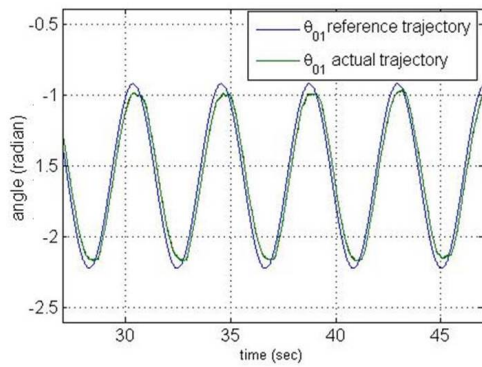
(a) x-axis of Separate Controller
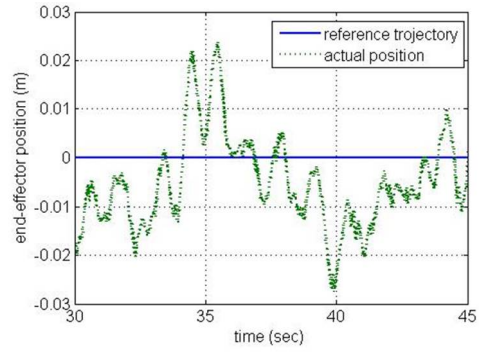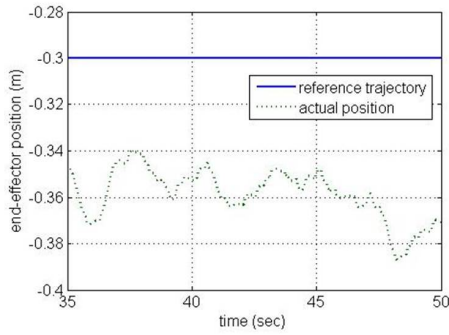
(b) x-axis of MOVA

(c) z-axis of Separate Controller
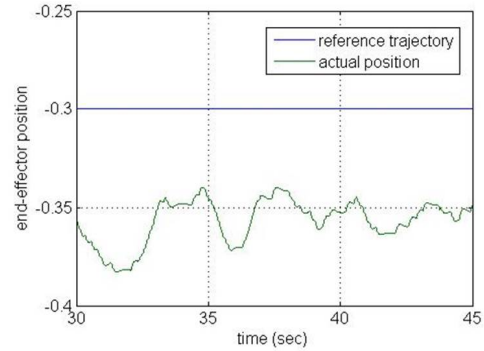
(d) z-axis of MOVA
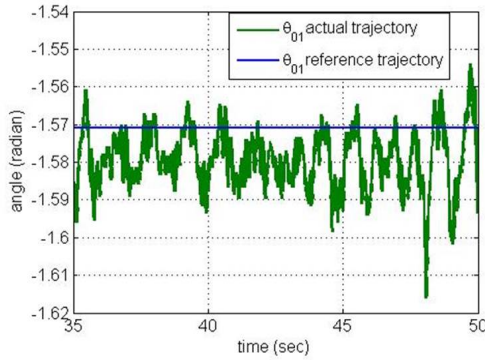
(e) θ_e of Separate Controller
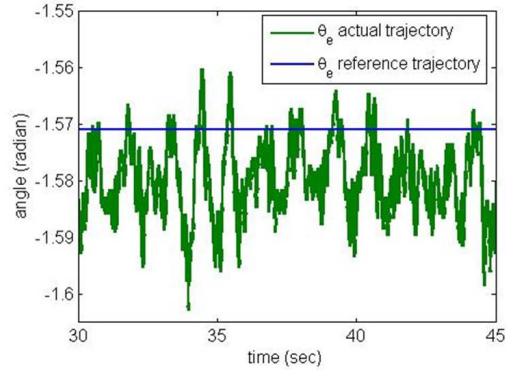
(f) θ_e of MOVA

Figure 3.2: Experiment 1, VTOL aircraft hovered at initial position

The second experiment is for the end-effector to track a desired trajectory while the VTOL hovers. The reference trajectory mimics a pendulum motion with range of $0.8 - \dfrac{\pi}{2}$ radian to $-0.8 - \dfrac{\pi}{2}$ radian while the host VTOL stays at a fixed

position defined as

$$p_{er} = \begin{bmatrix} 0 \\ 0 \end{bmatrix} \text{ mm.} \tag{3.38}$$

The desired end-effector position trajectory and direction are defined as

$$\theta_{01r}(t) = 0.8 sin(1.5t) - \frac{\pi}{2}$$
$$P_{er} = \begin{bmatrix} l_1 cos\theta_{01r}t \\ l_1 sin\theta_{01r}t \end{bmatrix}. \tag{3.39}$$

The experimental results are reported in Figure 3.3.
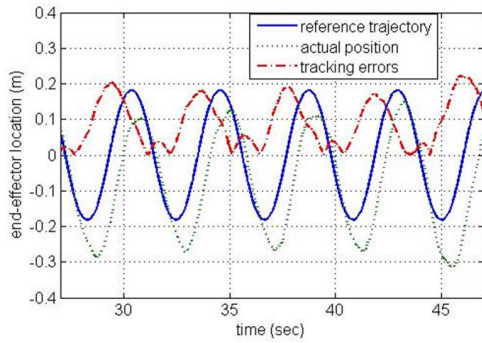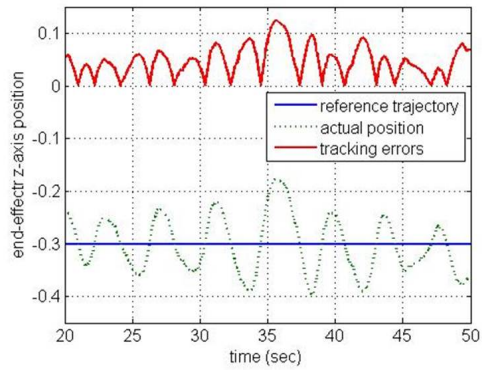
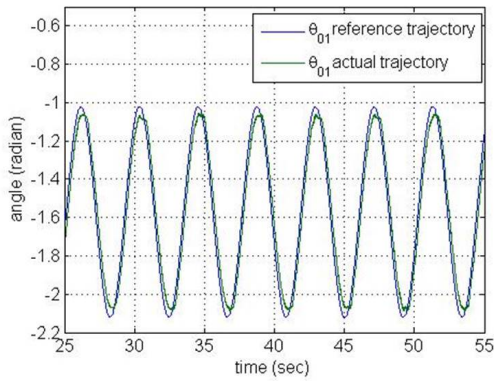(a) x-axis of Separate Controller
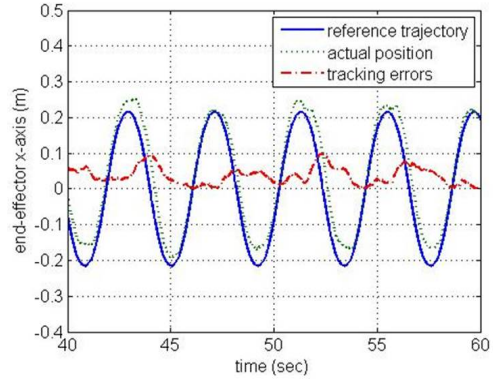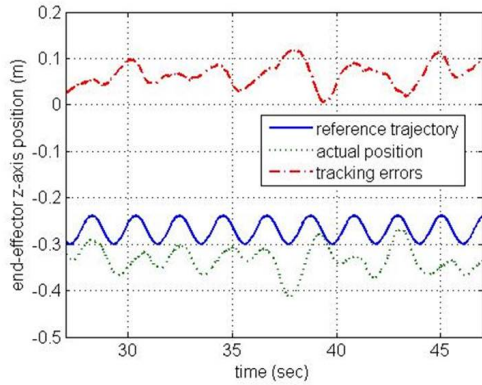
(b) x-axis of MOVA

(c) z-axis of Separate Controller

(d) z-axis of MOVA

(e) θ_e of Separate Controller
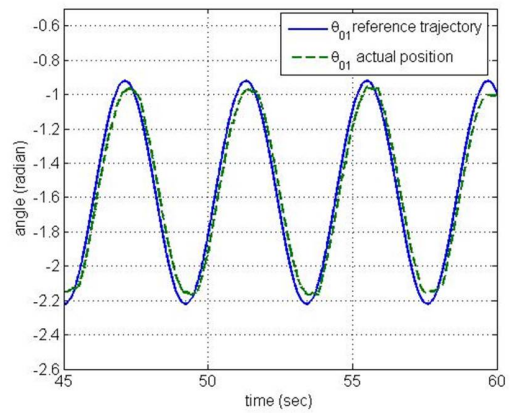
(f) θ_e of MOVA

Figure 3.3: Experiment 2, tracking pendulum motion trajectory

74

In the third experiment a reference trajectory of inverted pendulum motion was input to the system, which is defined as:

$$P_{er} = \begin{bmatrix} 0 \\ -0.25 \end{bmatrix} \text{ m}$$

$$\theta_{01r}(t) = 0.8 sin(1.5t) - \frac{\pi}{2}.$$

(3.40)

It is analogous to fastening a hexagon head bolt with a ratcheting wrench that the simulated robotic arm is a wrench operated by the VTOL (Figure 3.4). The trajectory is more difficult to perform in terms of the throttle control. The test evaluates the accuracy of the static thrust mapping in Chapter 2. Figure 3.5 presents the results.
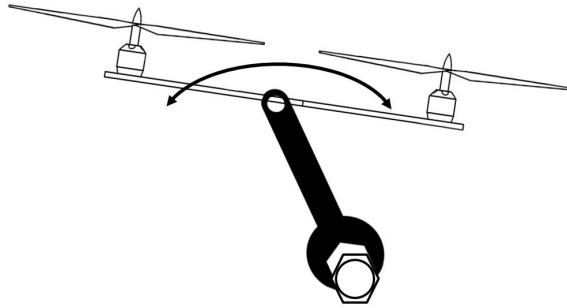
Figure 3.4: An illustration of the "wrenching a bolt" trajectory
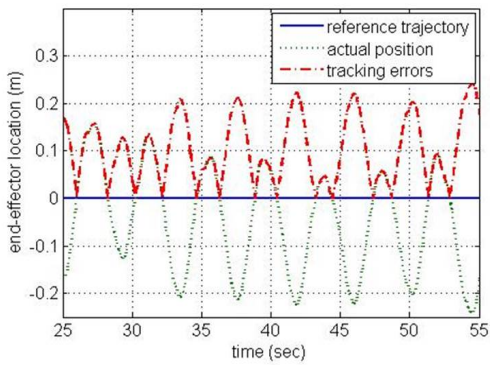
(a) x-axis of Separate Controller
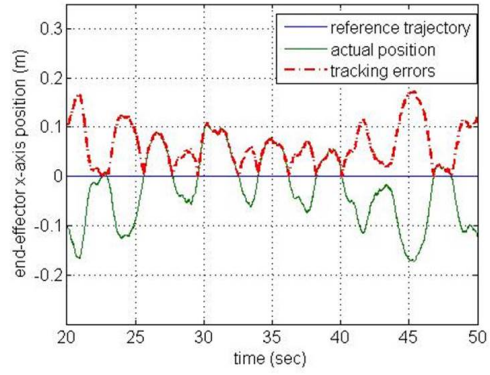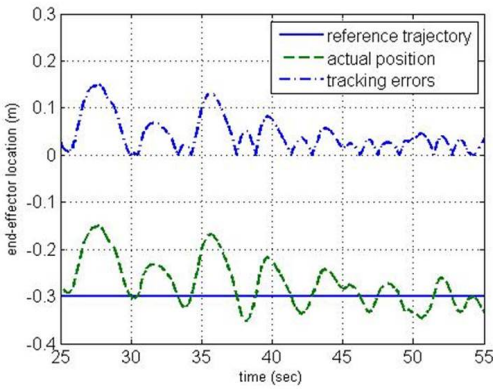
(b) x-axis of MOVA

(c) z-axis of Separate Controller

(d) z-axis of MOVA

(e) θ_e of Separate Controller
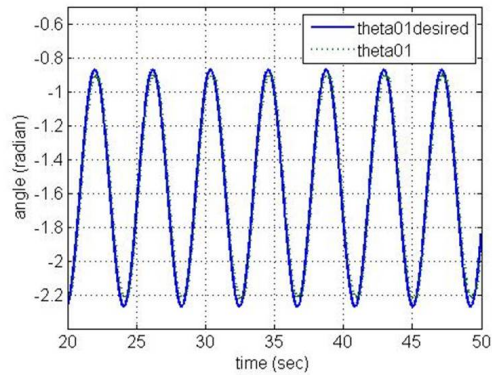
(f) θ_e of MOVA

Figure 3.5: Experiment 3, tracking inverted pendulum motion trajectory

3.3 Summary

In the first experiment, tracking a fixed location, the behavior of both systems are similar. Errors of x_e both remain below 5 centimeters, while the position errors projected to the z- axis have a constant error of about 0.05 m. It is partially due to the deteriorating performance of the motors after constantly running at full throttle for a long period of time.

In Experiment 2, a sinusoidal pattern was formed in the Separate Controller actual position projected to the x- axis, which results in fluctuating errors in the range from 0 m to 0.2 m. The errors may relate to the disturbance introduced by the manipulator to the system. The VTOL was "dragged" away by the shifted center of gravity of the manipulator and was only able to correct the position passively. On the other hand, active attitude changes of host VTOL were observed in MOVA system. The moves partially cancel out the systems internal torque, demonstrating the active compensation for interaction between manipulator and VTOL. The MOVA showed satisfying performance by keeping the x_e errors within 0.1 m. The results strengthen the claim that the planar MOVA controller takes into account the interactions between manipulator and the VTOL aerial vehicle.

In Experiment 3, the θ_{01} errors in both system are small as in the preceding tests. But the MOVA position tracking errors had seemingly increased. This can be improved by refining mapping from ESC PWM signal to the static thrust, or further designing a throttle controller based on propeller aerodynamics.

Chapter 4

Conclusions

A planar test bed, which consists of an instrumented tether and an experimental, 3 DOF planar UAV and single-link manipulator system, for UAV controller evaluation was presented in this thesis. A recently designed unified controller of a Manipulator On the VTOL Aircraft (MOVA) was validated. The test bed design process followed the top-down functional decomposition method. All components of the test bed were described and necessary details for replicating the test bed were provided. The propulsion modules were characterized based on the results of the frequency response tests. Two methods of VTOL attitude measurement, the encoder mechanical feedback via the tether and camera vision feedback, were explored. Performance tests were conducted on the test bed using both methods of feedback and the encoder was determined to be a better choice of sensor due to the better performance in this specific system.

The MOVA dynamics derivation based on the virtual manipulator method and the unified controller was briefly discussed. A modified controller, referred to as the Separate Controller, which removes the coupling compensation for the arm-UAV interaction, was designed for performance comparison. Both the MOVA system

and the Separate Controller were validated through experiments and the results were compared. The tests on the Separate Controller showed the negative impact of manipulator interaction on VTOL flying trajectory when tracking a reference end-effector trajectory. The MOVA unified controller, on the other hand, was able to actively compensate for the interaction and provided more refined tracking motion.

In summary, the test bed design met the need to produce a physical demonstration of the 2D MOVA controller. The instrumented tether can be used with other VTOL aircraft and the test bed as a whole can be used to test other control algorithms.

The system performance could be improved by replacing the components suggested in Table 4.1 to reduce the overall weight. Future research can be directed on developing a manipulator with grasping function and studying adaptive control design techniques to automatically tune the system parameters when the manipulator is interacting with other objects.

Current components	Replacement
TRD-S2500 Optical encoder	Triple axis gyroscope [18]
Hollow fiberglass tube in tether	Carbon fiber tube [23]
Ball bearings that connect the airframe and the tether	Ball bearing guide bushing [20]

Table 4.1: Recommended components

Appendices

Appendix A   Results of Static Thrust Test

Motor A					
Thrust (gram)	Speed (r/s)	PWM duty cycle (ms)	Thrust (gram)	Speed (r/s)	PWM duty cycle (ms)
20.27719	36	1.2	395.6524	89	1.48
40.05981	41	1.22	417.166	91	1.49
60.83156	45	1.24	436.2068	93	1.5
84.07614	48	1.26	450.7965	96	1.51
107.568	51	1.28	469.8372	98	1.52
129.3289	56	1.3	489.6199	101	1.53
142.1876	62	1.31	501.984	103	1.54
154.5517	64	1.32	521.7666	104	1.55
164.443	65	1.33	541.5492	107	1.56
176.8072	66	1.34	556.3862	108	1.57
189.6659	67	1.35	578.6417	110	1.58
200.0518	68	1.36	593.4786	113	1.59
211.9213	71	1.37	610.7884	115	1.6
226.7583	72	1.38	620.6797	116	1.61
237.1442	74	1.39	637.9895	118	1.62
247.2828	75	1.4	655.2993	120	1.63
263.1089	77	1.41	665.1906	121	1.64
276.9567	78	1.42	692.3917	123	1.65
294.2665	80	1.43	712.1743	125	1.66
316.5219	81	1.44	717.12	126	1.67
333.8317	83	1.45	741.8483	129	1.68
356.0872	85	1.46	744.3211	129	1.69
375.8698	87	1.47			

Table 2: Static thrust test results for motor A

Motor B					
Thrust (gram)	Speed (r/s)	PWM duty cycle (ms)	Thrust (gram)	Speed (r/s)	PWM duty cycle (ms)
16.81523	35	1.2	393.1796	89	1.48
35.60872	40	1.22	415.435	91	1.49
54.64949	44	1.24	435.2177	92	1.5
77.89407	47	1.26	452.5274	94	1.51
98.9131	50	1.28	472.3101	99	1.52
122.8995	56	1.3	492.0927	101	1.53
134.7691	59	1.31	504.4568	103	1.54
149.1115	62	1.32	524.2394	105	1.55
158.261	64	1.33	541.5492	107	1.56
173.0979	66	1.34	558.859	108	1.57
185.4621	67	1.35	578.6417	110	1.58
196.0952	68	1.36	593.4786	113	1.59
208.9539	70	1.37	610.7884	115	1.6
222.5545	72	1.38	623.1526	116	1.61
229.973	73	1.39	642.9352	119	1.62
243.5735	75	1.4	652.8265	120	1.63
259.6469	76	1.41	672.6091	122	1.64
274.4839	78	1.42	687.4461	123	1.65
294.2665	80	1.43	699.8102	124	1.66
314.0491	81	1.44	712.1743	125	1.67
331.3589	83	1.45	731.957	128	1.68
353.6143	85	1.46	741.8483	129	1.69
375.8698	87	1.47			

Table 3: Static thrust test results for motor B

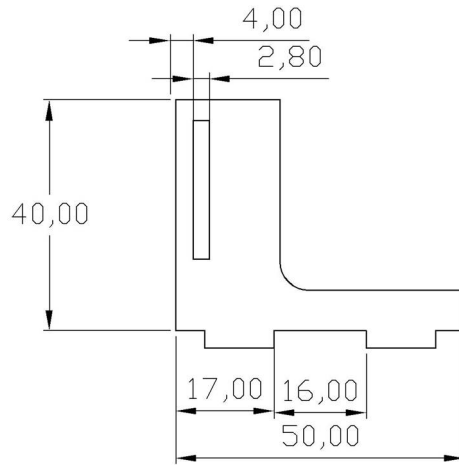# Appendix B   CAD Drawings of the Encoder Bracket
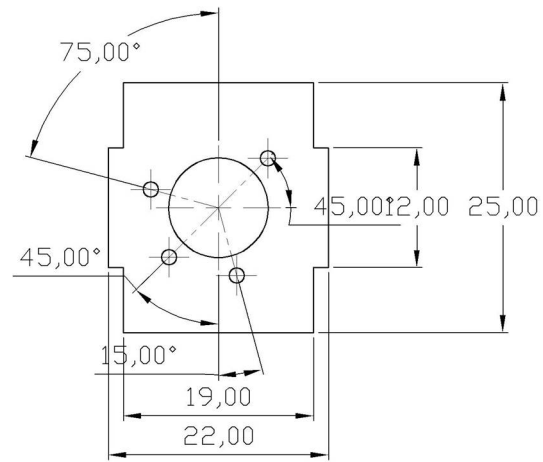

Figure 1: Side part of encoder bracket
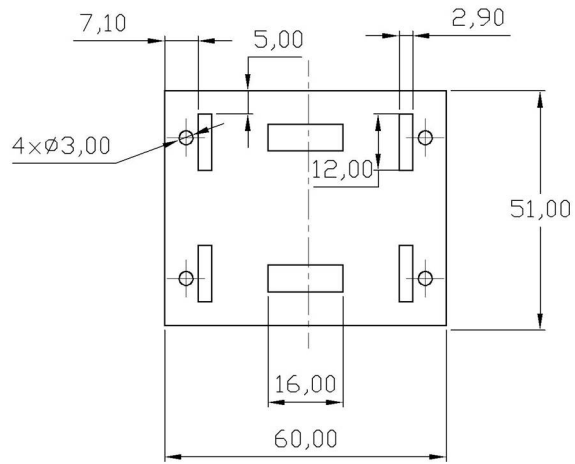

Figure 2: Front part of encoder bracket
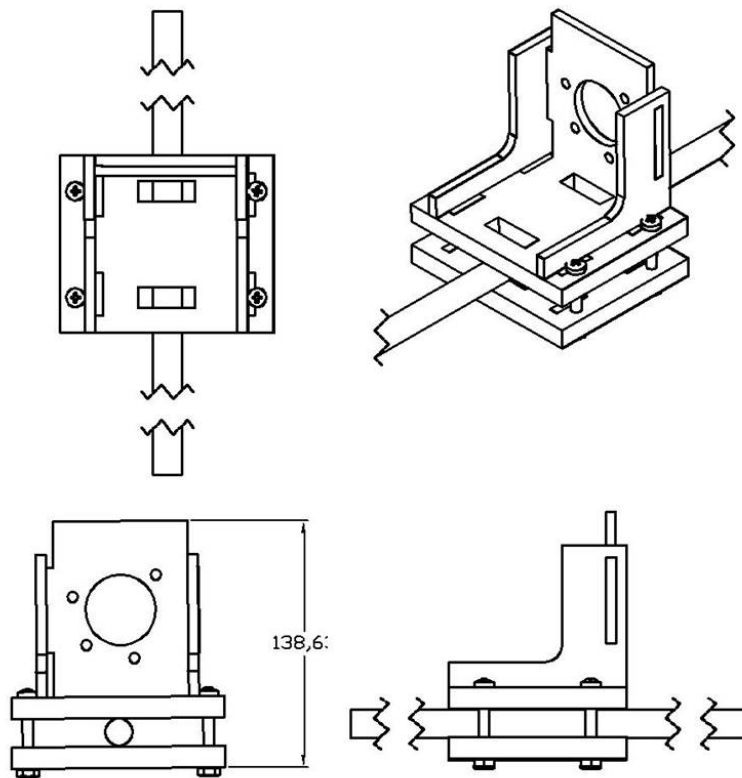
Figure 3: Base part of encoder bracket

Figure 4: Encoder bracket assembly drawing

Bibliography

[1] T.W. Danko and P.Y. Oh, "Design and Control of a Hyper-Redundant Manipulator for Mobile Manipulating Unmanned Aerial Vehicles," *Journal of Intelligent & Robotic Systems*, vol. 73, no. 1, pp. 709 - 723. Jan. 2014.

[2] F. Hoffmann, N. Goddemeier, and T. Bertram,"Attitude estimation and control of a quadrocopter," in *IEEE/RSJ Int. Conf. on Intelligent Robots and Systems*, Taipei, TW, 2010, pp. 1072 1077.

[3] A.E. Jimenez-Cano, J. Martin, G. Heredia, A. Ollero, and R. Cano, "Control of an aerial robot with multi-link arm for assembly tasks," *IEEE Int. Conf. on Robotics and Automation (ICRA),* Karlsruhe, DEU, 2013, pp. 4916 - 4921.

[4] C.M. Korpela, T.W. Danko, and P.Y. Oh, (Jan 2012) "MM-UAV: Mobile Manipulating Unmanned Aerial Vehicle," *Journal of Intelligent & Robotic Systems*, vol. 65, no. 1, pp. 93 101.

[5] M. Lungu and R. Lungu, "Adaptive backstepping flight control for a miniUAV," *Int. Journal of Adaptive Control and Signal Processing*, vol. 27, no. 8, pp. 635 - 650.

[6] N. Michael, D. Mellinger, Q. Lindsey, and V. Kumar, "The GRASP Multiple Micro-UAV Testbed," *IEEE Robot. Automat. Mag.*, vol. 17, no. 3, pp. 56 - 65.

[7] C. Nicol,, C.J.B. Macnab, and A. Ramirez-Serrano, . "Robust adaptive control of a quadrotor helicopter," in *Mechatronics*, 2011, vol. 21, pp.927 - 938.

[8] P.E.I. Pounds, D.R. Bersak, and A.M. Dollar, "Grasping From the Air: Hovering Capture and Load Stability," in *IEEE Int. Conf. on Robotics and Automation.* 2011, pp. 2491 - 2498.

[9] A. Tayebi and S. McGilvray, "Attitude stabilization of a VTOL quadrotor aircraft," in *IEEE Transactions on Control Systems Technology*, 2006, vol. 14, no. 3, pp. 562 571.

[10] X. Wu, Y. Liu, J. Zhu, "Design and real time testing of a trajectory linearization flight controller for the "Quanser UFO"," in *Proc. IEEE American Control Conference*, Mar. 2003, Vol. 5, pp. 3913 - 3918.

[11] YS. Yu and XL. Ding, "A Quadrotor Test Bench for Six Degree of Freedom Flight," *Journal of Intelligent & Robotics System*, vol. 68, no. 3-4, pp. 323 338, Dec. 2012.

[12] P. Xu, R. Huang, D. Lee, and T. Burg, "Dynamics and Control of a Novel MOVA System - A Planar Case Study," in *Proc. IEEE American Control Conference*, 2014.

[13] D. Lee, C. Nataraj, T. Burg, and D. Dawson, "Adaptive Tracking Control of an Underactuated Aerial Vehicle," in *Proc. IEEE American Control Conference*, 2011, pp. 2326 - 2331.

[14] P. Xu, "Unified Dynamics and Control of a Robot Manipulator Mounted on a VTOL Aircraft Platform," Ph.D. dissertation, Dept. Elect. Eng., Clemson Univ., Clemson, SC. 2014.

[15] S. K. Y. Nikravesh, *Nonlinear systems stability analysis: Lyapunov-based approach.* CRC Press, 2013.

[16] LAAS-CNRS. (2003) [Online; accessed July 2014]. Available: `http://homepages.laas.fr/matthieu/robots/h2bis.shtml`

[17] Oscar. (2013, October). How to choose Motor and Propeller for Quadcopter and Multicopter. [Online]. Available: `http://blog.oscarliang.net/how-to-choose-motor-and-propeller-for-quadcopter/`

[18] Sparkfun Electron. (2014) Triple-Axis Digital-Output Gyro. [Online; accessed May 2014]. Available: `https://www.sparkfun.com/products/11977`

[19] HobbyKing. (2014) Carbon fiber tube. [Online; accessed July 2014]. Available: `http://hobbyking.com/hobbyking/store/__43706__Carbon_Fiber_Tube_hollow_3x2x750mm_USA_warehouse_.html`

[20] Amazon. (2013) LM 10UU Linear bearing ball bushing. [Online; accessed June 2014]. Available: `http://www.amazon.com/LM10UU-Bearing-Bushing-Printer-MendelMax/dp/B00EO7GX42/ref=sr_1_1?ie=UTF8&qid=1406227540&sr=8-1&keywords=LM+10UU+Linear+bearing+ball+bushing`

[21] Pololu. (2014) Metal gear motor. [Online; accessed July 2014]. Available: `http://www.pololu.com/product/1445`

[22] Wikipedia. (2014, July) Aluminum. [Online]. Available: `http://en.wikipedia.org/wiki/Aluminium`

[23] Clearwater Composites, LLC. (2014) Properties of Carbon Fiber. [Online; accessed July 2014]. Available: `http://www.clearwatercomposites.com/`

[24] Wikipedia. (2014, June) Poly (methyl methacrylate). [Online]. Available: `http://en.wikipedia.org/wiki/Poly(methyl_methacrylate)`

[25] Q. C. Inc. (2003) Q8 data acquisition system user's guide. [Online]. Available: `http://www.clemson.edu/ces/crb/ece495/References/manuals/quanserq8manual.pdf`